The Dissertation Committee for Richard J. Hennessy
certifies that this is the approved version of the following dissertation:

# Depth Resolved Diffuse Reflectance Spectroscopy

Committee:

Mia K. Markey, Supervisor

James W. Tunnell, Co-Supervisor

Andrew K. Dunn

Stanislav Emelianov

Ammar M. Ahmed

# Depth Resolved Diffuse Reflectance Spectroscopy

**by**

**Richard J. Hennessy, B.S., M.S.**

**DISSERTATION**

Presented to the Faculty of the Graduate School of

The University of Texas at Austin

in Partial Fulfillment

of the Requirements

for the Degree of

**DOCTOR OF PHILOSOPHY**

THE UNIVERSITY OF TEXAS AT AUSTIN

May 2015

To Tracy, I love you.

# Acknowledgments

It is an honor to thank the following people who helped make this dissertation possible:

My family, Rick, Mary Jo, Debby, Keegan, and Jordyn for their support, encouragement, and love.

My committee members, Stas Emelianov, Andy Dunn, and Ammar Ahmed for working closely with me and providing advice.

The numerous mentors that I have been lucky to work with including Steve Jacques, Dan Gareau, Lily Laiho, Rafael Jimenez, Wensheng Fan, and Kristen Maitland.

Finally, I was extremely fortunate to have two wonderful supervisors: Drs. Mia K. Markey and James W. Tunnell. Their willingness to give me the freedom to pursue my doctoral work as I wanted as well as their expertise, advice, and support really allowed me to enjoy my time at UT Austin and has prepared me for a long and successful career. It was truly a privilege to work with both of you.

# Depth Resolved Diffuse Reflectance Spectroscopy

Richard J. Hennessy, Ph.D.
The University of Texas at Austin, 2015

Supervisor: Mia K. Markey
Co-Supervisor: James W. Tunnell

This dissertation focuses on the development of computational models and algorithms related to diffuse reflectance spectroscopy. Specifically, this work aims to advance diffuse reflectance spectroscopy to a technique that is capable of measuring depth dependent properties in tissue.

First, we introduce the Monte Carlo lookup table (MCLUT) method for extracting optical properties from diffuse reflectance spectra. Next, we extend this method to a two-layer tissue geometry so that it can extract depth dependent properties in tissue. We then develop a computational model that relates photon sampling depth to optical properties and probe geometry. This model can be used to aid in design of application specific diffuse reflectance probes. In order to provide justification for using a two-layer model for extracting tissue properties, we show that the use of a one-layer model can lead to significant errors in the extracted optical properties. Lastly, we use our two-layer MCLUT model and a probe that was designed based on our sampling depth model to extract tissue properties from the skin of 80 subjects at

5 anatomical locations. The results agree with previously published values for skin properties and show that can diffuse reflectance spectroscopy can be used to measured depth dependent properties in tissue.

# Table of Contents

# List of Tables

# List of Figures

# Chapter 1

# Introduction

## 1.1 Diffuse Reflectance Spectroscopy and Applications

Diffuse reflectance spectroscopy (DRS) is a technique that uses light to non-invasively measure the optical properties of tissue. In DRS, light is injected into the tissue, undergoes scattering and absorption, and a portion of light is reemitted to the surface and collected for analysis (see Figure 1.1). The collected light is called the diffuse reflectance, and this light contain quantitative information about the tissue's structure, compositions, and biochemical properties. DRS has been used in many different biomedical applications including tissue diagnostics for cervical cancer [1], breast cancer [2], oral cancer [3], lung cancer [4], esophageal [5] and gastrointestinal cancer [6], as well as monitoring of therapeutic procedures [7].

## 1.2 Instrumentation

A typical setup for measuring reflectance spectra consist of a broadband light source, a flexible optical fiber probe to direct the light to the tissue and collect the reemitted light, and a spectrometer to disperse and detect the measured signal. A computer is used to control the spectrometer and store

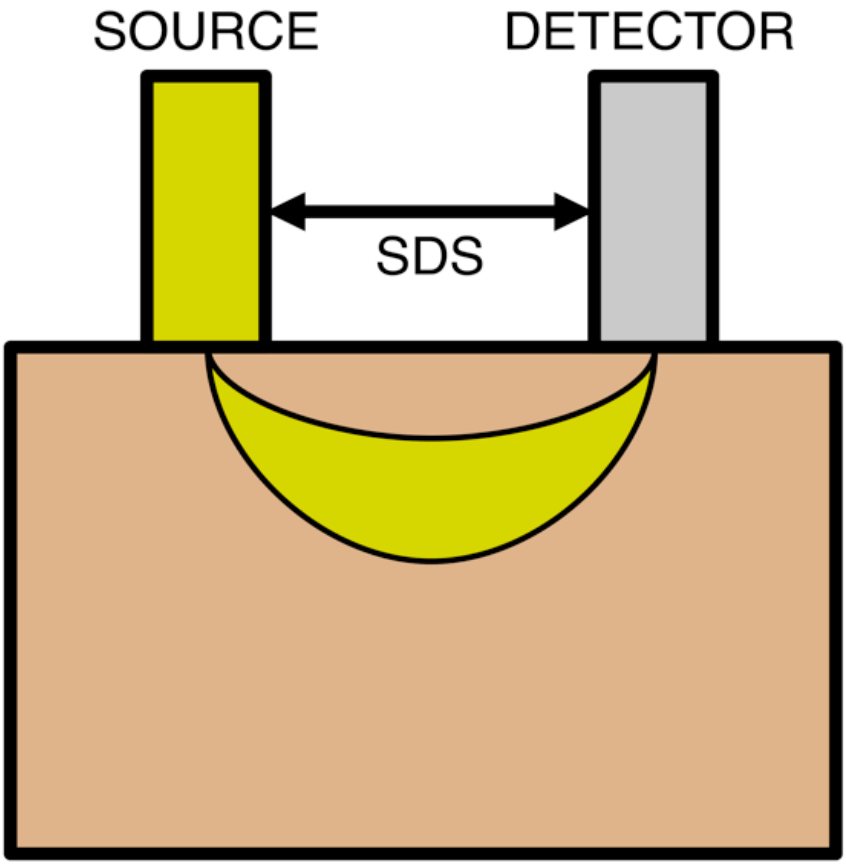


Figure 1.1: This is a simplified schematic of how a typical diffuse reflectance spectroscopy system works. Light is injected into the tissue and at some distance from the source, called the source-detector separation (SDS), the reflected light is detected.

the collected signal.

In addition to having inexpensive and simple instrumentation, another advantage of DRS is that it can be performed quickly and noninvasively. Additionally, the simple instrumentation used in DRS can easily be modified for specific applications. The most common DRS system uses a fiber based probe where one or more fibers connected to the light source is placed in contact with the tissue and delivers light to the tissue. At a distance from the source, called the source detector separation (SDS), is another set of fibers that collects the reflected light and sends it to the spectrometer for analysis. While the instrumentation for DRS is very simple, the accurate extraction of optical properties from the collected signal provides a significant challenge. A computational model is needed to relate the collected signal to tissue properties.

## 1.3 Modeling and Data Analysis

### 1.3.1 Scattering Coefficient

The two wavelength-dependent optical properties used to describe the scattering and absorption properties of tissue are the scattering coefficient ($\mu_s(\lambda)$) and the absorption coefficient ($\mu_a(\lambda)$). The scattering of light in tissue is not isotropic (having an equal probability of scattering in any direction), but is strongly in the forward direction. Because of this, scattering in tissue is often described using the reduced scattering coefficient ($\mu'_s(\lambda)$). Using the anisotropy factor ($g(\lambda)$), $\mu'_s(\lambda)$ can be calculated as shown in Equation 1.1.

$$\mu_s'(\lambda) = \mu_s(\lambda)[1 - g(\lambda)]. \tag{1.1}$$

The anisotropy factor ($g(\lambda)$) is a measure of the forward direction retained after a scattering event and is equal to the average cosine of the scattering angle.

Over a wide range of values for tissue properties, the decrease in $\mu_s'(\lambda)$ as a function of wavelength has been shown to be well described by a power law. The single power law shown in equation 1.2 has been widely used to describe $\mu_s'(\lambda)$.

$$\mu_s'(\lambda) = \mu_s'(\lambda_0) \left( \frac{\lambda}{\lambda_0} \right)^{-B} \tag{1.2}$$

The two parameters, $\mu_s'(\lambda_0)$ and $B$, can be extracted to describe the tissue scattering properties when the wavelength dependence of scattering is modeled using Equation 1.2. $\mu_s'(\lambda_0)$ is related to the magnitude of scattering and $B$ is related to the size of the scatterers.

### 1.3.2 Absorption Coefficient

The Beer-Lambert law (Equation 1.3) describes the attenuation of light that has passed through a non-scattering, absorbing solution.

$$I(\lambda) = I_0(\lambda) e^{-\varepsilon(\lambda) c L} \tag{1.3}$$

Where $I_0$ is the initial intensity of the light, $\varepsilon$ is the extinction coefficient of the absorber, $c$ is the concentration of the absorber, and $L$ is the path length (the distance the light travels through the absorbing solution). The absorption parameter, $\mu_a(\lambda)$, can be calculated by using Equation 1.4 for when there are multiple absorbers.

$$\mu_a(\lambda) = \sum_{i=1}^{N} \varepsilon_i(\lambda) c_i \tag{1.4}$$

Where $N$ is the number of absorbers, $\varepsilon_i(\lambda)$ is the wavelength dependent extinction coefficient of absorber $i$, and $c_i$ is the concentration of absorber $i$. The concentration values $c_i$ can be extracted to describe the absorption properties of the tissue. A model of light transport is needed to separate and quantify the absorption and scattering coefficients. Many of these models are based on the radiative transport equation.

### 1.3.3 Radiative Transport Equation

The radiative transport equation (RTE) describes the propagation of light through a medium in terms of a conservation law that accounts for gains and losses of photons due to scattering and absorption. The specific intensity, $I(r, \hat{s})$, is the intensity at position $r$ in the direction $\hat{s}$ and obeys the radiative transport equation which is shown in Equation 1.5.

$$\hat{s} \cdot \nabla I + (\mu_a + \mu_s) I = \mu_s \int p(\hat{s}, \hat{s}) I(r, \hat{s}') d\hat{s}' \tag{1.5}$$

where $\mu_a$ and $\mu_s$ are the absorption and scattering coefficients and $p$ is the phase function. The RTE can only be solved numerically and requires simplifications in order to obtain a closed form solutions. One such solution is the diffusion approximation.

### 1.3.4 The Diffusion Approximation

The diffusion approximation is a solution to the RTE that assumes light transport is dominated by scattering (minimal absorption) and that scattering is isotropic [8]. In tissue, scattering is not isotropic, so to satisfy this assumption, $\mu_s'$ is used instead of $\mu_s$. By correcting scattering using $g$, it can be treated similarly to isotropic scattering. In addition to isotropic scattering, there must be a sufficiently large number of scattering events before the photon is absorbed in order for the diffusion approximation to be valid. A commonly used rule to ensure that the diffuse approximation is valid is that $\mu_s'/\mu_s$ should be greater than 10. For probe based systems, the SDS must be greater than 1 or 2 transport mean free paths which is defined as $1/[\mu_s' + \mu_a]$. For many medical applications, such as measuring the properties of highly absorbing tissue, or applications that require short SDSs, the diffusion approximation is not valid. In these cases, computational methods, such as Monte Carlo simulation, can be used.

### 1.3.5 Monte Carlo Simulations

Monte Carlo (MC) simulation is a computational technique that can be used to provide an exact solution to the RTE. In the MC method, a large number of photons ($> 1 \times 10^7$) are launched into a medium that is defined by it's geometry, index of refraction, $\mu_s$, $\mu_a$, scattering phase function, and $g$ [9]. During the simulation, "photons" are injected into the tissue and the step size is determined based on the selection of a random number [0,1] and the local attenuation coefficient of the medium. At the end of each step, the weight of the photon is reduced by absorption. The photon is then redirected by a scattering event with the direction determined by a random number and the phase (or scattering) function. Once the trajectory is calculated, the photon is then moved a random distance and the whole process repeats (see Figure 1.2). Monte Carlo simulations can be time consuming because of their computational intensity and the large number of photons required to achieve a solution without significant stochastic noise.

### 1.3.6 Inverse Models

The models for light transport previously described are examples of forward models. A forward model is where the model parameters are defined *a priori* and then the output is data. In a typical real-world application, you have data that's been collected and you'd like to determine the model parameters. To solve this type of problem you need what is called an inverse model. For non-linear inverse problems, an iterative optimization algorithm

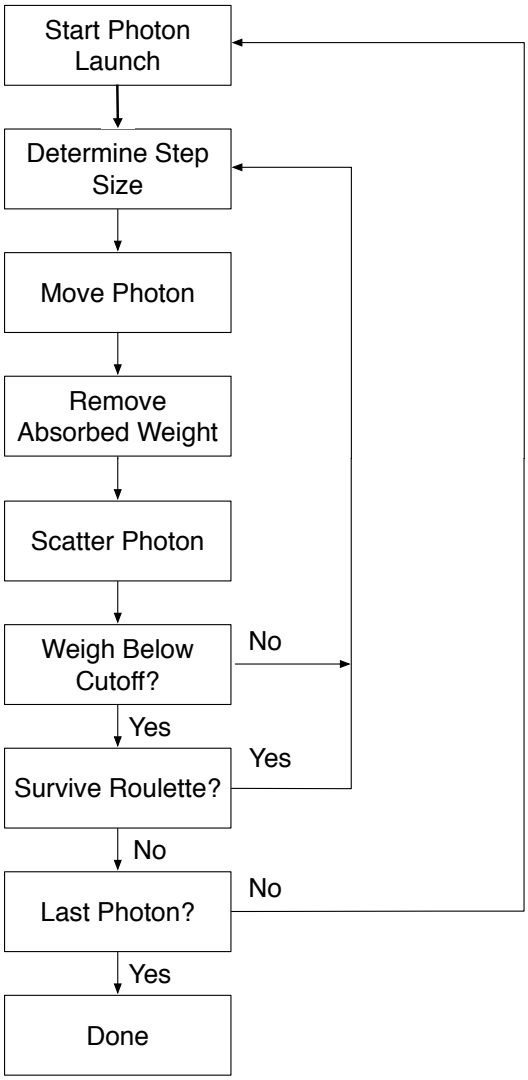


Figure 1.2: Flow chart of the Monte Carlo simulation for photon transport.

can be used to find a solution. Typically, these work by first making an initial guess, computing the error, and making more guesses until the error is minimized or some other criteria has been met. Because these optimization techniques are iterative, and depending on the dimensionality of the problem can take a lot of iterations, it's necessary that the computational intensity of each iteration is minimal. This is one reason for the limited application of Monte Carlo simulations in inverse models.

## 1.4 Outline of Thesis

In applications with highly absorbing tissues where short SDSs are necessary, the diffusion approximation is not valid and Monte Carlo simulation must be used to model light transport. However, the computational intensity of Monte Carlo simulations and the use of iterative techniques required for solving inverse problems presents a serious problem when trying to extract model parameters from clinical data. In Chapter 2, we present a solution to this problem based on what we call the Monte Carlo lookup table method. In this method, Monte Carlo simulations are run over a range of optical property combinations, then the values are saved in a lookup table so that they can be referred to when using the inverse model. This allows for significant speedup compared to running the Monte Carlo simulations during the inverse model and also provides the accuracy that comes with using Monte Carlo simulations. This technique was validated using optical phantoms and was found to be extremely accurate [10].

Most models of tissue used in DRS assume that the tissue is homogeneous (i.e. one-layer). In reality, tissue is composed of multiple layers with different optical properties. One example is skin, where you have the epidermis (containing melanin) and the dermis (containing hemoglobin). The use of a homogenous model in these cases can lead to significant errors in the extracted properties. Additionally, using a multi-layered model allows for the extraction of depth-dependent optical properties, which can provide diagnostically useful information. In Chapter 3, we extend the Monte Carlo lookup table method to two-layers. This is accomplished by increasing the dimensions of the lookup table so that a second layer in included [11].

One of the main findings from the two-layer model discussed in chapter 3 is that the accuracy of the extracted parameters was highly dependent on the thickness of the top-layer. This is due to the limited sampling depth of the probe that we used for the measurements. You can only measure the properties of a medium if light has passed through that medium. So when the top layer was very think, the errors for the bottom layer properties were high, and when the top layer was very thin, the errors for the top layer were very high. Based on this finding, we wanted to determine the relationship between the geometry of a DRS probe, the optical properties of the tissue, and the sampling depth of this photons. This was done in Chapter 4 using a combination of experimental, computational, and analytical approaches [12].

As discussed in Chapter 3, using a homogenous model to analyze DRS spectra can lead to errors in the extracted properties. In Chapter 5 we explore

this idea in detail. This is accomplished by first creating modeled spectra using a physiologically realistic two-layer model of skin and then using a homogeneous model to extract the properties from those spectra. We can then compare the parameters used to create the two-layer spectra to the extracted parameters and determine the specific errors caused by using a one-layer assumption [13].

In Chapter 6, the work described in the previous chapters is applied to *in vivo* DRS skin data collected from 80 different subjects on 5 different anatomical locations. The Monte Carlo lookup table method described in Chapters 2 and 3 is used to analyze the data. The depth sampling work described in Chapter 4 was used to aid in the design of a specialized probe made for skin applications. The depth dependent properties extracted from the *in vivo* data agreed with published results of the properties of skin. These results are promising, and show that DRS has potential to be used for measuring depth dependent properties in tissue for clinical applications.

# Chapter 2

# One-Layer Monte Carlo Lookup Table Model

This chapter is modified from "Monte Carlo lookup table-based inverse model for extracting optical properties from tissue-simulating phantoms using diffuse reflectance spectroscopy" published in The Journal of Biomedical Optics, 2013[1] [10].

## 2.1 Background

Diffuse reflectance spectroscopy (DRS) has been widely used to characterize tissue optical properties for disease diagnosis [6, 14–16]. Typically, DRS uses a fiber to deliver light to tissue. The delivered light is both scattered and absorbed by the tissue and is then recollected by another fiber a short distance from the source fiber. The collected light, or diffuse reflectance, contains quantitative information about tissue structure and composition. While the instrumentation for a DRS system is very simple, the accurate extraction of optical properties from the collected signal is a significant challenge. An

[1] **R. Hennessy**, S.L. Lim, M.K. Markey, & S.W. Tunnell, "Monte Carlo Lookup Table-Based Inverse Model for Extracting Optical Properties from Tissue Simulating Phantoms Using Diffuse Reflectance Spectroscopy." Journal of Biomedical Optics, 18(3), 037003 (March 2013). R. Hennessy developed the computational model. S.L. Lim performed the experimental work. M.K. Markey and J.W. Tunnell were advisors.

accurate tissue model is needed to relate the collected signal to tissue optical properties. One method for analyzing diffuse reflectance spectra relies on the solution to the diffusion approximation of the radiative transport equation. However, the diffuse approximation is not valid for short source-detector separations or in highly absorbing tissue [8].

Because most cancers originate in the epithelial layer, it is necessary to use probes with a short source-detector distance in order to sample photons that travel primarily through the epithelial layer [1]. Additionally, angiogenesis, an indicator of early cancer, can cause a significant increase in absorption due to blood. Unfortunately, the diffusion approximation is not valid in these regimes. Recently, reflectance lookup tables have been used to analyze diffuse reflectance spectra [17, 18]. These lookup tables are created in two different ways: experimental measurements of phantoms with known optical properties [17] or Monte Carlo simulations [19]. Creating a lookup table (LUT) with experimental measurements has the advantage of incorporating unknown system responses into the LUT. However, the creation of an experimental LUT is time-consuming, and the accuracy is dependent on the skill and experience of the investigator. The Monte Carlo method is especially useful from creating an LUT, because it provides the ability to model complex probe geometries and tissue structures. However, intensive computation is required to achieve results with desirable variance, which can make it extremely time-consuming to populate an LUT containing thousands of values.

Much prior work has been undertaken to improve the speed and ef-

ficiency of the Monte Carlo method for modeling light transport in turbid media. These methods can be separated into three groups:

1. methods that use the information from a small set of Monte Carlo simulations and scale the results to calculate a wide range of optical properties [20],

2. methods that use geometry splitting techniques to increase the fraction of useful photons [21], and

3. methods that parallelize the Monte Carlo simulations [22].

The first set of methods has the advantage of not requiring a large number of simulations to create and LUT. However, errors arise because the photon trajectory information necessary to perform the scaling operation can be recorded only in several depth intervals with finite widths [23]. Geometry splitting techniques decrease the number of photons need for a simulation to converge, but their implementation is very difficult for complex probe geometries. The third set of methods uses classical Monte Carlo simulations and therefore does not make any sacrifices in accuracy, flexibility, or implementation difficulty. Speedup is achieved by simulating multiple photons simultaneously on different processors. Because each photon is independent of every other photon, this problem is considered "embarrassingly parallel." Alerstam et al. have shown that general-purpose graphic processing units (GPGPUs) can increase the speed of Monte Carlo simulations of photon transport by

three orders of magnitude on a relatively inexpensive GPU when compared to the sequential implementation [22]. We present, for the first time, a Monte Carlo LUT (MCLUT) based model where all values in the LUT were created by independent Monte Carlo simulations by using a parallel implementation on a GPGPU.

## 2.2 Creation of the Lookup Table

A two-dimensional Monte Carlo code written in ANSI C implemented on an NVIDIA GTX 560 Ti GPU with NVIDIA's Compute Unified Device Architecture (CUDA) was used to simulate photon reflectance in a single-layer tissue model on 386 parallel threads [22]. The multiply with carry random number generator was used. The refractive index above the tissue was set to 1.452 to match the refractive index of the fiber, and the refractive index of the tissue was set to 1.33 to match the refractive index of the phantoms. To test the effect of errors in the refractive index, we created LUTs with different refractive indices and repeated the extraction of optical properties with the different LUTs. We found a 5% error rate in the refractive index corresponds to error increases of 1.3% for extracted $\mu_s'$ values and 0.8% for extracted $\mu_a$ values. To prevent photons from exiting the tissue volume, the radius and width of the tissue volume were set to 3 cm. A total of $1 \times 10^6$ photons were launched to obtain the impulse response. To ensure stochastic noise would be sufficiently low in LUT location with high albedo, 100 separate MC simulations were performed with the optical properties that would

give the lowest value of reflectance. We found that using $1 \times 10^6$ photons reduced the standard deviation of the 100 different reflectance values to less than 0.5% of the mean. The diffuse reflectance for our specific probe geometry was then calculated by convolving the impulse response with the beam profile [24]. Our probe was modeled using a Gaussian sapped beam profile of collimated light with a diameter of 200 μm, a detector diameter of 200 μm, and a source-detector separation of 250 μm. The diffuse reflectance values for all physiologically realistic combinations of scattering and absorption were calculated using the GPGPU Monte Carlo implementation with the tissue and probe geometry described above. Twenty evenly spaced increments were used for both scattering (0 to 50 $cm^{-1}$) and absorption (1 to 50 $cm^{-1}$), meaning a total of 400 separate Monte Carlo simulations were needed to create the LUT. The Henyey-Greenstein phase function was used for sampling scattering angles. The scattering anisotropy ($g$) was set to 0.85 for all simulations. For the range of $g$ values present in human tissue ($g > 0.8$), it has been shown [20] that the diffuse reflectance will be the same for any values of $\mu_s$ and $g$ that generate the same $\mu_s'$. The resulting MCLUT is shown in Figure 2.1. It took 2 minutes to run the 400 separate Monte Carlo simulations.

## 2.3 Forward and Inverse Models

For the forward model used to generate diffuse reflectance spectra, the reduced scattering coefficient was contained to the form

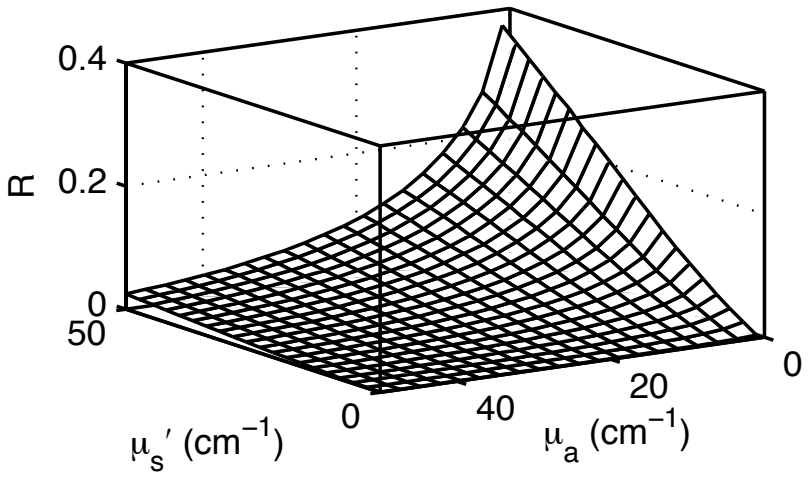


Figure 2.1: The resulting lookup table $[R(\mu_s', \mu_a)]$ created using 400 separate Monte Carlo simulations. Each Monte Carlo simulation was used to calculate a reflectance value for a given scattering coefficient and absorption coefficient.

$$\mu_s'(\lambda) = \mu_s'(\lambda_0) \times \left(\frac{\lambda}{\lambda_0}\right)^{-B} \tag{2.1}$$

where $\lambda_0 = 630$ nm. The absorption coefficient was calculated using

$$\mu_a(\lambda) = \sum_{i=1}^{N} \ln 10 \varepsilon_i(\lambda) C_i \tag{2.2}$$

where $\varepsilon_i(\lambda$ is the wavelength-dependent extinction coefficient of a chromophore, $C_i$ is the concentration of that chromophore, and $N$ is the number of chromophores. Depending on the type of tissue sampled and the wavelength range of interest, any number of chromophores can be used to calculate $\mu_a(\lambda)$. Once $\mu_s'(\lambda)$ and $\mu_a(\lambda)$ are calculated, the MCLUT can be used to generate a modeled

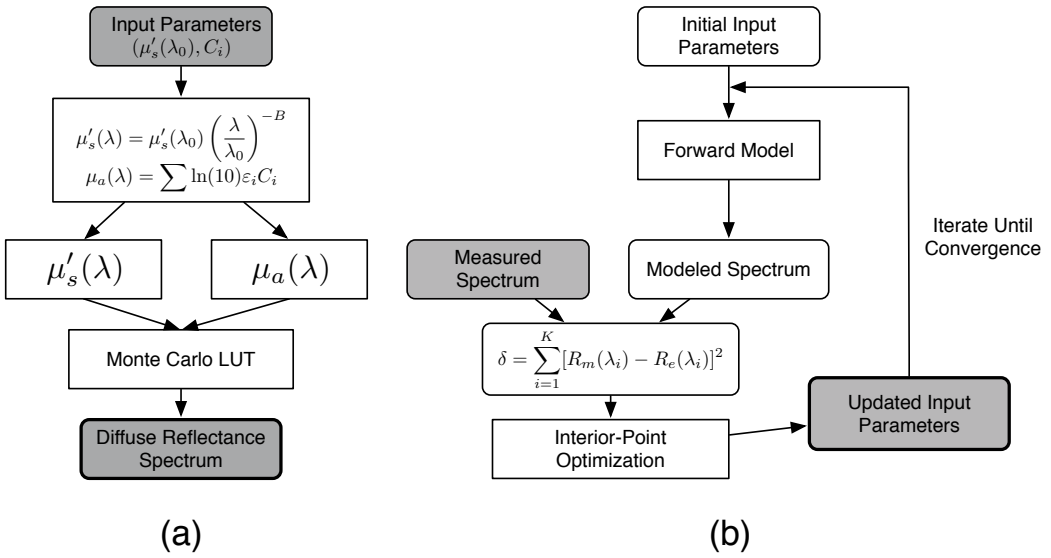


Figure 2.2: Flowcharts for the (a) forward and (b) inverse models of one-layer diffuse reflectance used to create modeled spectra and to fit the MCLUT model to the reflectance data.

reflectance spectrum. Cubic splines were used to interpolate between values in the LUT. Figure 2.2(a) shows the forward model of diffuse reflectance.

Figure 2.2(b) shows the inverse model used to fit our diffuse reflectance spectra. First, we made an initial guess for the optical properties, and then the forward model was used to generate a spectrum. Next, the sum of squares error between the predicted reflectance and the measured reflectance was calculated using

$$\delta = \sum_{i=1}^{K} \left[R_m(\lambda_i) - R_e(\lambda_i)\right]^2, \tag{2.3}$$

where $\delta$ is the sum of squares error, $K$ is the number of wavelength points, $R_m$

is the measured spectrum, $R_e$ is the modeled spectrum, and $\lambda_i$ is the wavelength. The parameters are then iteratively updated until the sum of squares error is minimized. An interior-point nonlinear optimization routine proved in the MATLAB optimization toolbox (Mathworks, Nattick, Massachusetts) was used as the optimization algorithm. The average fit time was 1.3 seconds, with the number of iterations limited to 5000 and the termination tolerance on the error function set to $1 \times 10^{-3}$. Because the modeled spectra are in absolute units (photons counted) and the measured spectra are in units relative to a baseline calibration measurement, it is necessary to perform a calibration so that the modeled spectra can be compared. Additionally, the calibration corrects for wavelength-dependent responses in the experiment that are not accounted for in our forward model. We performed the calibration by taking the ration of a modeled spectrum and a measured spectrum with the same optical properties. Then, to make the measured spectra equivalent to the modeled spectra all measured spectra were multiplied by this ratio. To ensure that the choice os optical properties used in the calibration step did not bias the results, the mean of the ratios for all spectra used in the validation set was used for calibration. The mean calibration ratio is shown in Figure 2.3.

## 2.4 Validation and Results

To test the performance of our MCLUT-based inverse model, we created 21 tissue phantoms with hemoglobin (Hb) (Sigma-Aldrich) as the absorber and polystyrene beads (diameter = 1 μm) as the scatterer. Hb concentra-

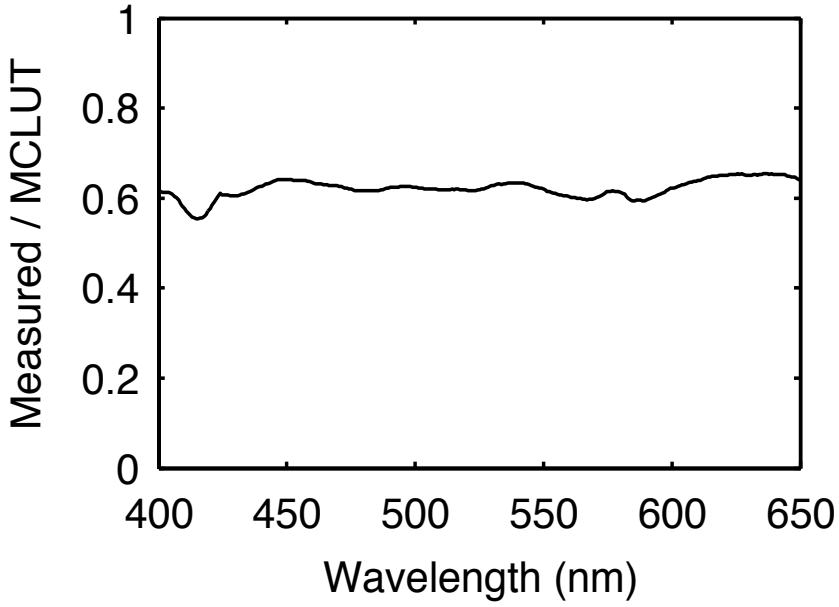


Figure 2.3: Mean of all ratios of measured and modeled diffuse reflectance spectra with the same optical properties. This ratio was used for calibration.

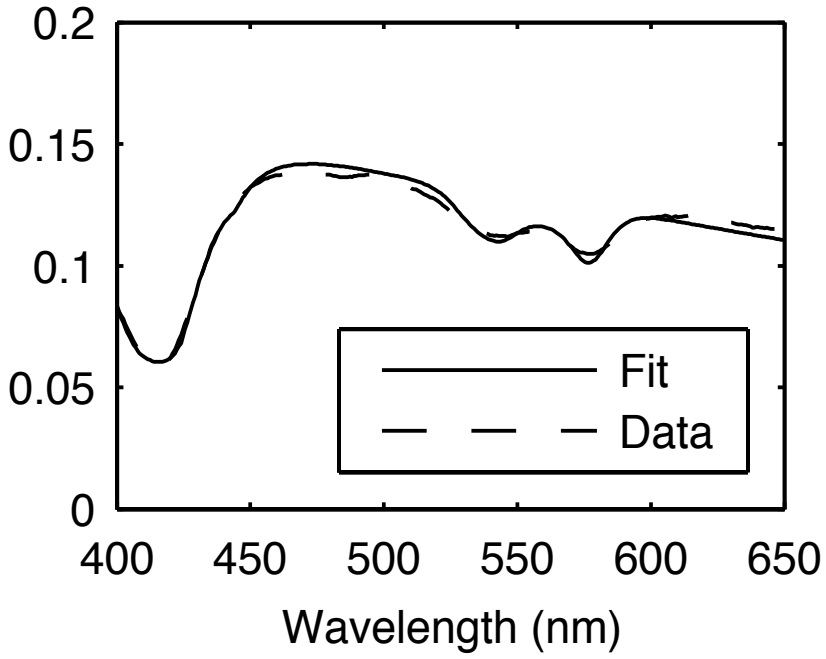


Figure 2.4: A diffuse reflectance spectrum (dashed) [$\mu_s'(\lambda_0) = 25.4$ cm$^{-1}$ and [Hb] = 1.5 mg/ml] and associated MCLUT-fit (solid).

tion ([Hb]) ranged from 0 to 3 mg/ml, and the reduced scattering coefficient $[\mu_s'(\lambda_0)]$ ranged from 6.4 to 27.5 $cm^{-1}$. We used Mie theory to calculate the $\mu_s'$ of the tissue phantoms. For our inverse model, we assumed the absorption in the visible range was due to oxyhemoglobin. We measured the optical density for the $HbO_2$ solution using a spectrophotometer and calculated the absorption spectrum using Beer's Law. Because the addition of $HbO_2$ dilutes the solution, a small change in $\mu_s'$ was accounted for when calculating the known values for $\mu_s'$. The DRS system consisted of a xenon flash lamp (Model: E6611, Hamamatsu) as the light source, a spectrograph (Model: SP2150i, Princeton Instruments) and camera (Cool-SNAP, Photometrics) as the spectrometer, and a fiber optic probe with the same geometry as described above (FiberTectOptica, Ontario, Canada). A diffuse reflectance spectrum and its associated fit can be see in Figure 2.4 and shows that the inverse model can accurately fit the experimental data.

Figures 4.2(a) and 4.2(b) show scatter plots of the extracted versus expected values for $\mu_s'(\lambda_0)$ and [Hb], respectively. The solid line in each plot is the line of perfect agreement. The results indicate that there is excellent agreement between the extracted and expected values. The MCLUT inverse model estimated the optical properties over a wide range with average root-mean-square percent errors of 1.74% for $\mu_s'$, 0.74% for $\mu_a$, and 2.42% for [Hb]. We compared the performance of our MCLUT-based model to an experimental LUT-based model. The MCLUT model was able to estimate $\mu_s'$ and $\mu_a$ with decreases is percent error magnitude of 3.16% and 10.86%, respectively, when

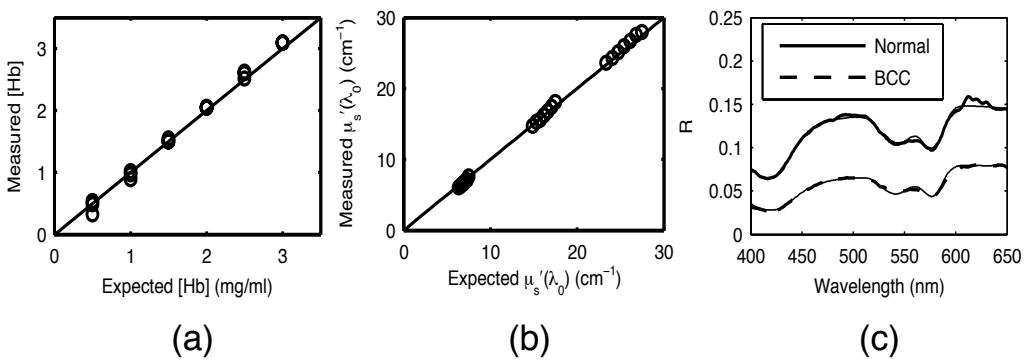


Figure 2.5: (a) Hemoglobin concentration extracted from the MCLUT inverse model versus known hemoglobin concentration. The solid line indicates perfect agreement. (b) $\mu_s'(\lambda_0)$ extracted from the MCLUT inverse model versus known $\mu_s'(\lambda_0)$. The solid line indicates perfect agreement. (c) *In vivo* reflectance spectra from two representative groups: clinically normal and basal cell carcinoma (BCC). The thin solid line ins the fit.

compared to the experimental LUT model [17].

Our inverse model was then tested on previously collected data from a clinical feasibility study [25] to illustrate the application of the mode for non-invasive detection of skin cancer. Figure 4.2(c) shows representative spectra from two groups: clinically normal and basal cell carcinoma (BCC). The plot shows good agreement between the MCLUT fit and the measured *in vivo* spectra. For this analysis, the absorption coefficient was determined using melanin, deoxygenated hemoglobin, and oxygenated hemoglobin as the absorbers.

## 2.5 Conclusions

Although other inverse models have recently been developed for extracting optical properties from diffuse reflectance spectra, this work represents the first Monte Carlo lookup table-based inverse model where the LUT was generated entirely by Monte Carlo simulations. Previously, the amount of time required to generate an LUT entirely by Monte Carlo simulations made this technique infeasible. However, recent advances in GPGPU computing have allowed parallel Monte Carlo implementations capable of running three orders of magnitude faster than traditional, serial implementations of Monte Carlo simulations. By creating an LUT entirely by Monte Carlo simulation, our method is not subject to the errors that arise from using either the diffusion approximation or the Monte Carlo scaling method. When compared to an experimental LUT, our method was more accuracy, but, more importantly, it has the advantages of being repeatable and easier to implement. This model can also be adapted to more complex probe and tissue geometries. In the next chapter, we extend the MCLUT method to a two-layer tissue geometry so that it can measure depth dependent properties.

# Chapter 3

# Two-Layer Monte Carlo Lookup Table Model

This chapter is modified from "Verification of a two-layer inverse Monte Carlo absorption model using multiple source-detector separation diffuse reflectance spectroscopy" published in Biomedical Optics Exress, 2013[1] [11].

## 3.1 Background

Diffuse reflectance spectroscopy (DRS) has been used to noninvasively measure tissue properties for skin-related disease diagnosis [14, 15, 25–27]. Typically, DRS uses a fiber to deliver light to tissue. The delivered light is both scattered and absorbed by the tissue and is then detected by another fiber, which is at a certain distance, known as the source-detector separation (SDS), from the source fiber. The diffuse reflectance spectra, calculated as the ratio of the collected light intensity to the delivered light intensity, contains quantitative information about tissue structure and composition. While the instrumentation for a DRS system is relatively straight forward, the accurate

[1] M. Sharma*, **R. Hennessy***, M.K. Markey, & J.W. Tunnell, "Verification of a two-layer inverse Monte Carlo absorption model using multiple source-detector separation diffuse reflectance spectroscopy." Biomedical Optics Express, 5(1), 40-53 (January 2014). **These authors contributed equally to this work.* R. Hennessy developed the computational model. M. Sharma performed the experimental work. M.K. Markey and J.W. Tunnell were advisors.

extraction of optical properties from the measured reflectance is a significant challenge. An accurate model of light transport in tissue is needed to relate the measured reflectance to tissue optical properties. One method for analyzing diffuse reflectance spectra is the diffusion approximation of the radiative transport equation; however, the diffusion approximation is not valid for short source-detector separations or in highly absorbing tissues [6, 8, 28].

Because many diseases are located in the epithelial layer at the tissue surface, it is necessary to use probes with a short SDS in order to sample photons that travel through the epithelial layer [1, 29]. Additionally, angiogenesis, an indicator of early cancer, can cause a significant increase in absorption due to blood. Many models of light transport in tissue have been developed to overcome this limitation. These include empirical models [30, 31], experimental models [17, 18], and computational models [9, 10, 19]. The majority of these models assume tissue to be a homogeneous semi-infinite turbid medium. However, many tissues have a layered structure and the homogeneity assumption can lead to errors in extracted optical properties [32]. Towards this end, two-layer models of diffuse reflectance have been developed in order to model light transport in two-layer tissues. Despite representing significant advances to the field, these models have several limitations including requiring the top layer thickness to be known *a priori* [33–35] and utility only for specific tissue types and probe geometries [23, 34–38].

Towards addressing these limitations, we present a two-layer Monte Carlo look-up table (MCLUT) model, extended from a single layer MCLUT

model previously developed by our group [10]. Briefly, the advantages of a MCLUT approach are its ability to work for a wide range of probe geometries and tissue types, the ease of implementation, and its speed. Our two-layer MCLUT inverse model is capable of extracting optical properties and top layer thickness from diffuse reflectance spectra. This current work aims to validate our two-layer model by comparing model predictions to experimental measurement for two different SDSs (370 and 740 μm) across a physiologically realistic range of optical properties and top layer thicknesses. Two SDSs were used because the 740 μm SDS will sample deeper than its 370 μm counterpart; it is the difference in reflectance spectra obtained from each SDS - due to the sampling depth variation - that aids in the accurate prediction of top layer thickness over a wider range of thicknesses. The ability of this technique to measure both morphological properties, such as top layer thickness, as well as functional properties, such as hemoglobin concentration, allows us to provide useful diagnostic information with application including (1) pigmentary disorder studies, (2) disease (rosacea, lupus, scleroderma, morphea, lymphedema) monitoring, (3) treatment outcome measures, (4) topical medical absorption studies, (5) thickness of psoriasis plaque, and (6) cosmetic studies.

## 3.2 Creation of the Monte CarloLookup Table

Photon transport in tissue was modeled using Monte Carlo simulation of a two-layer model with four free parameters: top layer thickness ($Z_0$), top layer absorption coefficient ($\mu_{a,t}$), bottom layer absorption coefficient ($\mu_{a,b}$)

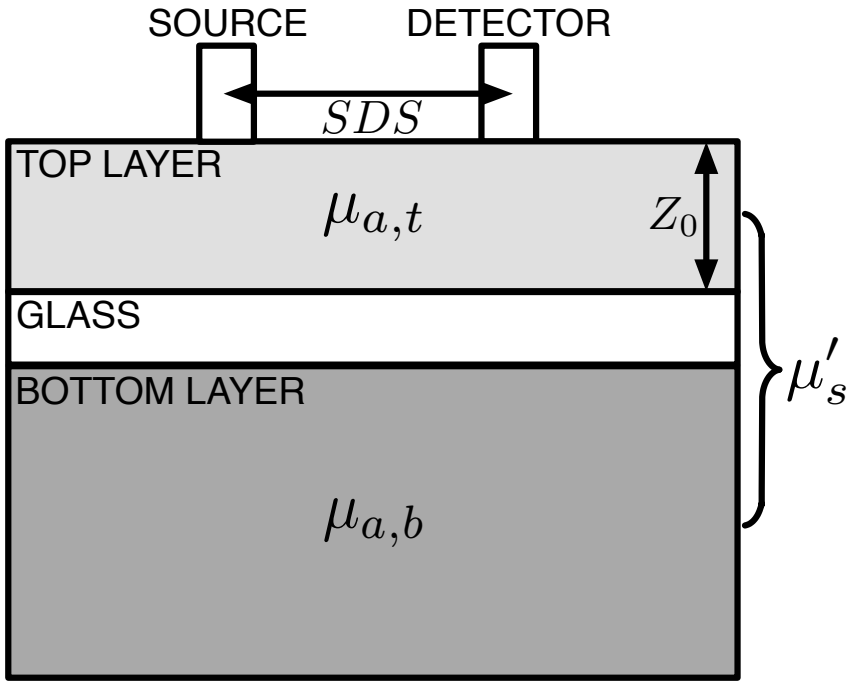


Figure 3.1: Two-layer model geometry used in the Monte Carlo simulations. Absorption for the top and bottom layers, scattering for both layers, and the top-layer thickness are used as inputs to generate reflectance values for all SDSs. The coverslip was modeled as a middle layer with constant thickness of .625 mm, no scattering or absorption, and an index of refraction of 1.5.

and the reduced scattering coefficient ($\mu_s'$), which is assumed to be the same for both layers. In reality, scattering can change from one layer to the next; however our simplifying assumption improves the convergence properties of the inverse model. Additionally, previous two layer models of diffuse reflectance have made this same assumption and shown the ability to accurately measure depth dependent absorption properties in the presence of scattering differences between layers [34, 35, 39]. Figure 3.1 shows the two-layer geometry of the model.

A two-dimensional Monte Carlo code written in ANSI C implemented on an NVIDIA GTX 560 Ti GPU with NVIDIA's Compute Unified Device Architecture (CUDA) was used to simulate photon reflectance in the two-layer tissue model on 386 parallel threads [22]. The multiply-with carry random number generator was used. The refractive index above the tissue was set to 1.452 to match the refractive index of an optical fiber, and the refractive index of the medium was set to 1.4 to match the refractive index of tissue. Spatially resolved diffuse reflectance was calculated by convolving the impulse response using a Gaussian shaped beam profile with a diameter of 100 μm [24]. We created two separate MCLUTs: one with an SDS of 370 μm, and one with an SDS of 740 μm, where each was modeled as concentric annuli in order to increase the number of detected photons. The coverslip used in the two layer phantoms was modeled as a middle layer with a constant thickness of .625 mm, no scattering or absorption, and an index of refraction of $n = 1.5$. Every entry in each MCLUT contains a reflectance value for a given $Z_0$, $\mu_{a,t}$, $\mu_{a,b}$, and $\mu_s'$. In the MCLUTs, $Z_0$ ranges from 0 to 3000 μm, $\mu_{a,t}$ ranges from 0 to 5 $\text{mm}^{-1}$, $\mu_{a,b}$ ranges from 0 to 5 $\text{mm}^{-1}$, and $\mu_s'$ ranges from 0 to 7 $\text{mm}^{-1}$. The ranges for the parameters were selected to cover a range larger than the optical properties used to create the phantoms in order to prevent biasing of the results. Twenty evenly spaced increments were used for each of the free parameters listed above, giving a total of 160,000 separate MC simulations. Cubic splines were used to interpolate between values in the MCLUT. A total of $1 \times 10^6$ photons were used for each MC simulation and

were found to sufficiently reduce stochastic noise below 2% for all values in the MCLUT; however, the error for the values in the MCLUT within the optical property range of the phantoms is below 0.2%. The Henyey-Greenstein phase function was used for sampling scattering angles. Scattering anisotropy, $g$, was set to 0.85 for all simulations. For the range of $g$ values present in human tissue ($g > 0.8$), it has been shown [20] that the diffuse reflectance will be the same for any combination of values of $\mu_s$ and $g$ that generate the same $\mu_s'$. For light transport near the source location (short SDSs) as employed in this study, previous look-up table studies conducted in our laboratory have shown that extracted absorption and reduced scattering coefficient values have less than 10% error when the anisotropy is greater than 0.7 [18]. Total time to create the MCLUTs was 16.2 hours.

## 3.3 Forward Model

A forward model of diffuse reflectance relates tissue optical and geometric properties to diffuse reflectance as described by the flowchart in Fig. 3.2. For our two-layer model, the properties of interest are top-layer ($\mu_{a,t}$) and bottom layer ($\mu_{a,b}$) absorption coefficients, top-layer thickness ($Z_0$), and reduced scattering coefficient ($\mu_s'$), which is assumed to be the same for both layers. Reduced scattering at all wavelengths is calculated using Equation 3.1, which is commonly employed for tissue optics.

$$\mu_s'(\lambda) = \mu_s'(\lambda_0) \times \left(\frac{\lambda}{\lambda_0}\right)^{-B}, \tag{3.1}$$

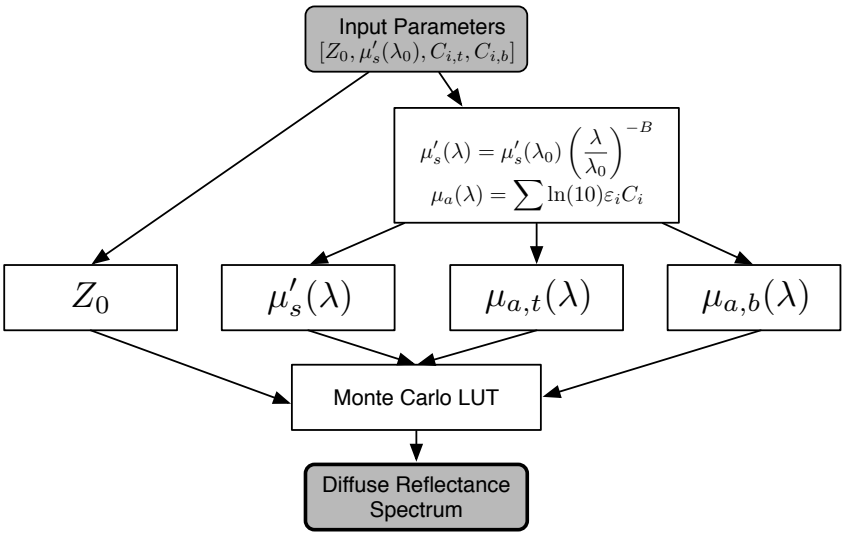


Figure 3.2: Flowchart for the forward model of diffuse reflectance for a two-layer tissue model. Tissue parameters are inputs into the model and the output is a diffuse reflectance spectrum. The Monte Carlo lookup table is used to determine reflectance based on the set of optical properties and top layer thickness.

where $\mu_s'(\lambda)$ is the reduced scattering coefficient at wavelength $\lambda$, $\lambda_0 = 630$ nm, and $B$ is the scattering exponent. The scattering exponent, $B$, was fixed to 1.5 and the selection of a value for $B$ was found to have negligible impact on the accuracy of extracted parameters because of the calibration procedure described in section 3.3. Absorption in the top layer at each wavelength is calculated using Equation 3.2.

$$\mu_{a,t}(\lambda) = \sum_{i=1}^{N_t} \ln(10)\varepsilon_{i,t}(\lambda)C_{i,t}, \tag{3.2}$$

where $\mu_{a,t}(\lambda)$ is the absorption coefficient at wavelength $\lambda$ in the top layer, $N_t$ is the number of chromophores in the top layer, $\varepsilon_{i,t}(\lambda)$ is the extinction coefficient at wavelength $\lambda$ of chromophore $i$ in the top layer, and $C_{i,t}$ is the concentration of chromophore $i$. Similarly, the absorption coefficients at each wavelength for the bottom layer are calculated using Equation 3.3.

$$\mu_{a,b}(\lambda) = \sum_{i=1}^{N_b} \ln(10)\varepsilon_{i,b}(\lambda)C_{i,b} \tag{3.3}$$

where $\mu_{a,b}(\lambda)$ is the absorption coefficient at wavelength $\lambda$ in the bottom layer, $N_b$ is the number of chromophores in the bottom layer, $\varepsilon_{i,b}(\lambda)$ is the extinction coefficient at wavelength $\lambda$ of chromophore $i$ in the bottom layer, and $C_{i,b}$ is the concentration of chromophore $i$. Once the optical properties are determined at each wavelength, the MCLUT is used to determine the reflectance at each wavelength and cubic splines used to interpolate between values in the MCLUT.

## 3.4 Inverse Model

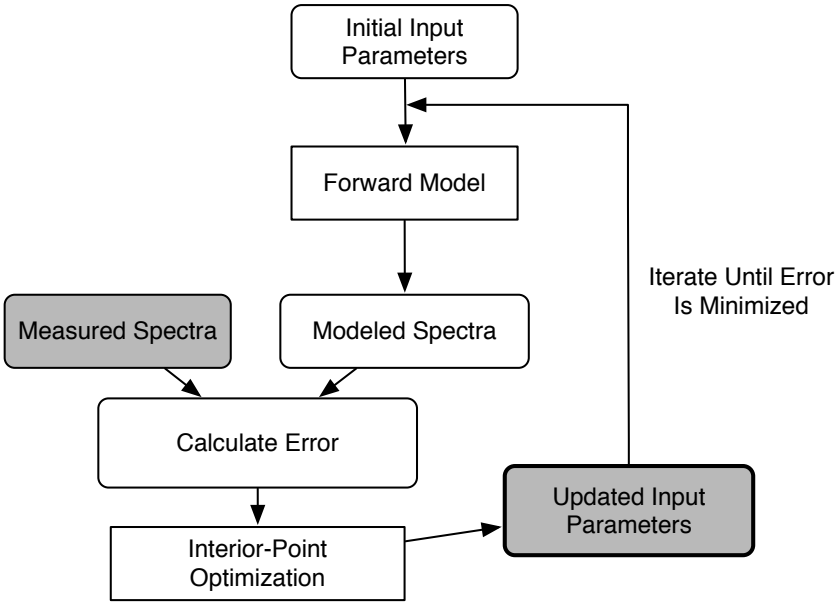


Figure 3.3: Inverse model of diffuse reflectance. First, an initial guess for the tissue parameters is used to generate a spectrum with the forward model. Next, the error between the measured and modeled spectra is calculated and the parameters are updated using an optimization routine that minimizes the error between the modeled and measured spectra.

While the forward model provides a useful tool for analyzing the effect of layered tissue geometry on diffuse reflectance, the real utility of the model is realized by inverting the model so that we can extract tissue properties from measured spectra. Fig. 3.3 illustrates the flowchart for the inverse model of diffuse reflectance in a two-layer tissue. This allows one to use the model in conjunction with a DRS system to characterize tissue and aid in disease diagnosis. The two-layer model that relates tissue properties to diffuse reflectance is non-linear and, therefore, cannot be directly inverted. One method is to

use an iterative optimization routine. This is achieved by first estimating an initial value for the tissue properties and using the forward model to generate an initial reflectance spectrum. The mean squared percent error between the measured spectrum and model spectrum is then computed using Eq. 3.4:

$$E = \frac{1}{nS} \sum_{S} \sum_{\lambda} \left[ \frac{R_{s,meas}(\lambda) - R_{s,model}(\lambda)}{R_{s,meas}(\lambda)} \right]^2 \tag{3.4}$$

where $E$ is the error, $n$ is the number of wavelength points, $S$ is the number of source detector separations, $R_{s,meas}(\lambda)$ is the reflectance of the measured spectrum at wavelength $\lambda$ and source detector separation $S$ (370 μm and 740 μm), and $R_{s,model}(\lambda)$ is the reflectance of the model spectrum at wavelength $\lambda$ and source detector separation $S$. Next, the tissue properties are updated using an interior-point optimization routine [40] from the MATLAB optimization toolbox to work towards minimizing the error. An initial guess of $Z_0 = 300$ μm, $\mu_{a,t} = 1$ mm$^{-1}$, $\mu_{a,b} = 1$ mm$^{-1}$, and $\mu_s' = 1.5$ mm$^{-1}$ was used for all spectra, and the choice of initial guess was found to have negligible impact on the final results. The average time to convergence is on the order of 1 second on an Intel Core i5 2.7GHz processor.

## 3.5 Experimental Validation

### 3.5.1 Two-Layered Phantoms

Experimental data for model verification were obtained by constructing two-layered phantoms. In total, 15 phantoms were constructed to cover the

Table 3.1: Summary of the optical properties of the two-layer phantoms used in this study for comparison with MC simulations. The scattering values are given for $\lambda = 630$ nm. For the absorbers: g is green dye; r is red dye; b is blue dye; and Hb is dissolved Hemoglobin powder. The largest source of uncertainty for the optical property values is due to errors in the pipette volumes required in order to create the liquid phantoms. The pipettes were calibrated; however, based upon vendor specifications, pipette volume uncertainties were calculated to result in approximately a 4% error in optical property values.

| Phantom Number | $\mu_s'(\lambda_0)$ ($\text{mm}^{-1}$) | $\mu_{a,t,max}$ ($\text{mm}^{-1}$) | $\mu_{a,b,max}$ ($\text{mm}^{-1}$) |
|---|---|---|---|
| 1 | 1.5 | 0.25 (b) | 1.275 (r) |
| 2 | 1.5 | 0.25 (r) | 1.275 (b) |
| 3 | 1.5 | 2.3 (b) | 0.25 (g) |
| 4 | 1.5 | 2.3 (g) | 0.25 (b) |
| 5 | 1.5 | 0.25 (b) | 2.3 (g) |
| 6 | 1.5 | 0.25 (g) | 2.3 (b) |
| 7 | 2.85 | 0.25 (r) | 2.3 (b) |
| 8 | 2.85 | 0.25 (b) | 2.3 (b) |
| 9 | 2.85 | 2.3 (r) | 0.25 (b) |
| 10 | 2.85 | 1.275 (g) | 0.25 (r) |
| 11 | 2.85 | 1.275 (g) | 2.3 (r) |
| 12 | 0.75 | 0.25 (r) | 2.3 (g) |
| 13 | 0.75 | 0.25 (r) | 2.3 (g) |
| 14 | 1.7 | 0 | 1 (Hb) |
| 15 | 1.54 | 0 | 1.5 (Hb) |

relevant range of optical properties [41, 42]. Table 3.1 summarizes their optical properties.

For Phantoms 1-13, food dyes were used as the absorbers for both the top and bottom layers, while phantoms 14-15 were designed to simulate physiological circumstances with a scattering top layer (epithelial layer) and an absorbing bottom layer containing hemoglobin (stromal layer). Each phantom

has the same top and bottom scattering properties, which is presented in terms of the reduced scattering coefficient at 630 nm, $\mu_s'(\lambda_0)$. The top and the bottom layer absorption properties differ in terms of concentration (maximum absorption co-efficient [$\mu_{a,t,max}$ and $\mu_{a,b,max}$]) and absorbing molecule. Polystyrene 1.025 μm diameter beads with 2.5% solid by volume (Polysciences, PA) were used as the scattering media; red, green and blue food dyes (Safeway, TX) and lyophilized hemoglobin powder (H0267, Sigma Aldrich, MO) were used as absorbers. The optical density for all absorbers was measured using a spectrophotometer (DU720, Beckman Coulter, CA.) and the absorption spectra were calculated using Beer's law.

Across all these phantoms, $\mu_s'$ ranges from 0.81-4.91 $mm^{-1}$ and the $\mu_a$ values range from 0-2.3 $mm^{-1}$. $\mu_{a,t,max}$ and $\mu_{a,b,max}$ represent the maximum absorption coefficient for top and bottom layers across all wavelengths, respectively. These values correspond to physiologically relevant values of cutaneous optical properties used for skin cancer and other dermatological purposes [25, 41, 42]. The $\mu_s'(\lambda_0)$ values were chosen and the resultant bead solution (beads + de-ionized water) volumes calculated using a Mie theory algorithm that evaluates the total scattering cross-section across the wavelength range 350-750 nm for each specified bead solution. Both the top and bottom layers were mixed in vials and thoroughly agitated in order to guarantee complete mixing.

As shown in Figure 3.4, each phantom consists of a bottom layer (encapsulated by a small vial cap and a glass coverslip) and a top layer. The

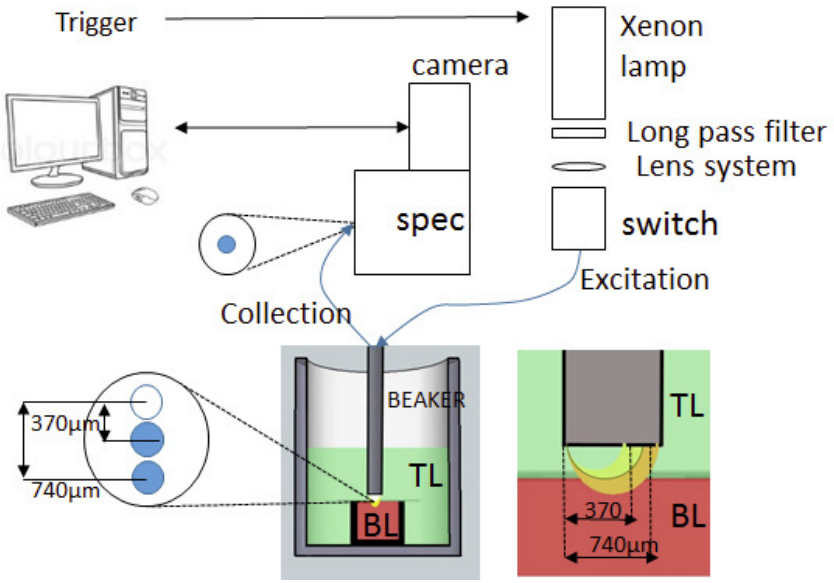


Figure 3.4: Schematic of the two-layered experiment and the DRS system used to collect the data, including the "photon flow" from: excitation provided by the xenon lamp, whose signal is passed through a long-pass filter and an optical lens system for collimation and focusing into a fiber-optic switch to be delivered to the two-layer phantom, consisting of a top layer (TL) and bottom layer (BL). The bottom layer is housed in a small vial cap with a coverslip placed on top, and the top layer poured on top of it. Collection is at 370 and 740 µm SDSs and passed into a spectrograph and imaged by a cooled CCD camera. Custom software provides the trigger for the light source and detector and also processes and stores the measured spectra for later analysis.

vial cap diameter was 19.05 mm; no change in spectra was observed between spectra taken in the center of the vial cap and 5 mm offset from the center, which confirmed that the vial cap was a semi-infinite medium and the vial side-wall was not causing photon attenuation or altering the photon path. The probe is mounted on a fine-scale translation stage with 5 μm resolution (Model 433, Newport, CA) such that it is centered about the vial cap and can be traversed vertically through the volume of the beaker. The bottom layer solution was pipetted into the inside of a small vial lid and capped off by affixing a 0.625 mm thick microscope coverslip to the outside rim of the lid using superglue. Once dry, this lid was then affixed to the internal base of a 30 mL beaker using superglue and care taken to ensure that the vial cap was as flat as possible. The probe was traversed downwards using the translation stage until flush. The top layer solution was then pipetted into the beaker. Small 4-40 screws were placed at the bottom of the beaker (but all below the microscope slide) in order to occupy as much volume as possible and save cost on the polystyrene beads. In each case, the height of the top layer (depth of liquid above microscope slide after top layer volume addition), was measured in order to ensure that the top layer was at least 2 mm deep. Prior to data collection, initial measurements were taken to ensure that no top layer liquid had seeped in between the probe tip and microscope slide.

### 3.5.2 Diffuse Reflectance Spectroscopy System

Reflectance measurements were made using a linear probe (FiberTech Optica, Canada), consisting of 15 fibers aligned side-by-side, each at a center-to-center separation of 370 μm. Excitation light was delivered through the central (7) fiber and light collected from fibers 8 and 9, corresponding to SDSs of 370 and 740 μm respectively. As shown in Fig. 3.4, the 740 μm SDS will sample deeper than the 370 μm and, as discussed previously, it is this difference in sampling depth between the two channels that enables top layer thickness measurements over a wide range. Measurements were taken at flush (0 μm, probe touching microscope slide) and subsequently at 50 μm increments until there was no change in reflectance across all wavelengths.

We used a pulsed Xenon flash lamp as the DRS light source (L7684, Hamamatsu Photonics, NJ), which provided broadband 375-700 nm illumination as identified in Fig. 3.4. The Xenon lamp provided a pulse of full width half maximum (FWHM) 2.9 μs. In order to prevent second-order dispersion contaminating the reflectance spectra, the Xenon white light was first passed through a 340 nm long-pass filter (Asahi Spectra, Torrance, CA). The light was then collimated and focused using two lenses. Per acquisition, the Xenon lamp was pulsed twice to deliver light for both the 370 and 740 μm SDSs. The two white light pulses are coupled into an optical fiber and guided into a $3 \times 1$ optical switch (FSM-13, Piezosystems Jena, Germany). The switch is a microelectromechanical (MEMS) device, which uses microprisms to control and open different optical ports to ensure that the two broadband Xenon light

pulses are separated and coupled sequentially into the linear probe without any overlap. The switch is controlled via transistor-transistor logic (TTL) pulse trains. Light from the switch's output was then passed to the input of the linear probe via a subminiature version A (SMA) nipple fitting; roughly 30% loss in signal is measured due to the optical switch and SMA fitting. The distal end of the linear probe was aligned with the vertical axis of the spectrograph (SpectraPro 2150i, Princeton Instruments, Trenton, NJ) using software provided by the manufacturer (WinSpec, Princeton Instruments, Trenton, NJ). A 150 grooves/mm grating, blazed at 500 nm, was used in order to capture the entire visible spectrum needed DRS (375-700nm). A slit width of 200 μm was used. All spectra were collected for an exposure time of 50 μs.

The data collection was controlled via custom software written in LabVIEW (National Instrument, Austin, Texas). The software executes two-layer data collection by sequentially capturing the 370 and 740 μm signals. Onboard calculations were performed to convert the raw signals into reflectance spectra (see Section 3.4). The Xenon pulsed lamp was triggered via TTL pulses provided by a timer-counter board (NI 2121, National Instruments, Austin, Texas). The camera was controlled by a PCI card (PCI-6602, National Instruments, Austin, Texas) and operated, in part, by pre-written software (R3 Software, Princeton, NJ). The timing of optical port switching was also controlled by TTL pulses sent by the custom software.

### 3.5.3 Calibration Measurements

For each phantom, wavelength calibration was performed using a mercury-argon light source (HG-1, Ocean Optics, FL) which provides clear, distinct atomic spectral lines. Because the modeled spectra are in absolute units (photons counted) and the measured spectra are in units relative to a calibration measurement, it was necessary to perform an additional calibration so that the modeled and measured spectra can be compared. Reflectance measurements were taken each day of a stock solution of polystyrene beads (no absorption) where $\mu_s'(\lambda_0) = 1.5\ \text{mm}^{-1}$ and then modeled spectra were calculated using the same optical properties as the stock solution. Next, the ratio of the measured to modeled spectra were calculated and all measured spectra were multiplied by this ratio. Additionally, the calibration corrects for wavelength dependent responses in the experiment that are not accounted for in the forward model, including the wavelength dependent response of the spectrograph, and the wavelength dependance of scattering anisotropy ($g$) and index of refraction ($n$).

### 3.5.4 Spectral processing

At each height, the final DRS spectrum per SDS is the average across five separate measurements (five pulses per height). To improve the SNR, we bin every three pixels for a final spectral dispersion of 0.77 nm/pixel and a resulting spectral resolution FWHM of 5.3 pixels (4.08 nm). We calculate the reflectance using Equation 3.5.

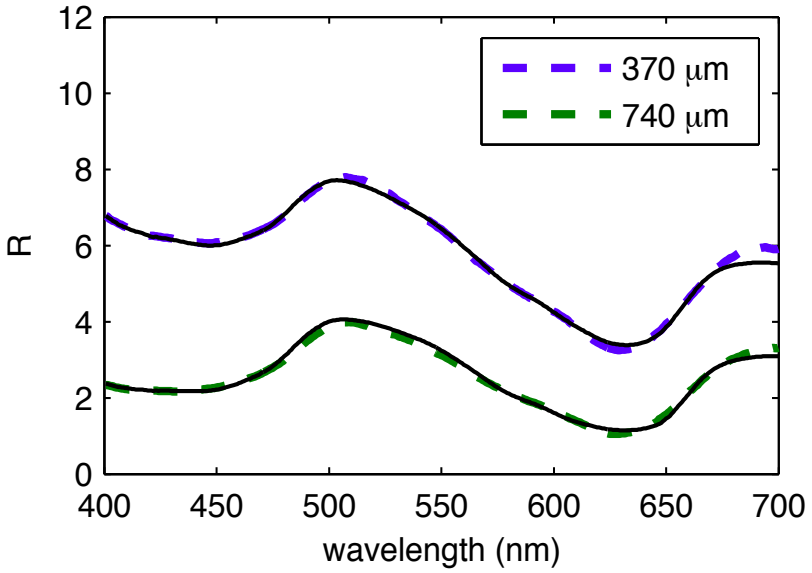


Figure 3.5: Measured spectra (colored and dashed) and associated MCLUT fits (solid black) from phantom 3 with a top layer thickness of 300 μm.

$$R(\lambda) = \frac{I_{sample}(\lambda) - I_{background}(\lambda)}{[I_{standard}(\lambda) - I_{background}(\lambda)] \times 100/R_{standard}} \tag{3.5}$$

where $I_{sample}(\lambda)$ is the raw spectrum from the phantom, $I_{background}(\lambda)$ is the background (spectra collected without the white light excitation), $I_{standard}(\lambda)$ is the spectralon standard spectra and $100/R_{standard}$ is used to account for the calibrated reflectance level of the spectralon standard (throughout this paper all results were obtained with a 20% spectralon reflectance standard). Spectra are presented in terms of wavelength by using the Hg-Ar lines to convert pixels to wavelength. Fig. 3.5 shows the measured spectra and associated MCLUT fits from phantom 3 with a top layer thickness of 300 μm.

## 3.6 Results and Discussion

Fig. 3.6 is included as a visual demonstration of how the reflectance spectra change with increasing $Z_0$ and of the increased sampling depth with increased SDS. Here spectra are shown at selected heights from phantom 8. Scaled absorption spectra of the red and blue dye are shown for reference. We see that at flush (0 μm) only the red dye is sampled. As the depth increases, the blue ink absorption becomes increasingly more pronounced; conversely, the red dye absorption decreases. These are consistent with physical intuition that increasing top layer thickness corresponds to increased top layer absorption and decreased bottom layer absorption. Finally, at 1000 μm, red dye absorption is barely detectable and only the blue ink top layer is being sampled. These trends are more evident for the 740 μm SDS as more dye molecules are sampled. The most dramatic change in the reflectance spectra occurs at reasonably shallow depths (from 250-600 μm).

The inverse model was used to extract optical properties ($Z_0$, $\mu_s'(\lambda_0)$, $\mu_{a,t,max}$, $\mu_{a,b,max}$) from all spectra across all phantoms. For each of these 4 variables, at each height up to 0.95mm, we computed the normalized root-mean-square-deviation ($NRMSD$) averaged across all 15 phantoms, which is calculated as shown in Equation 3.6.

$$NRMSD = \frac{1}{x_{i,max} - x_{i,min}} \sqrt{\frac{\sum_{i=1}^{n} \left(x_i(Z_0) - \hat{x}_i(Z_0)\right)^2}{n}} \tag{3.6}$$

where $x$ is the variable of interest, $i$ is the phantom number, $n$ is the total

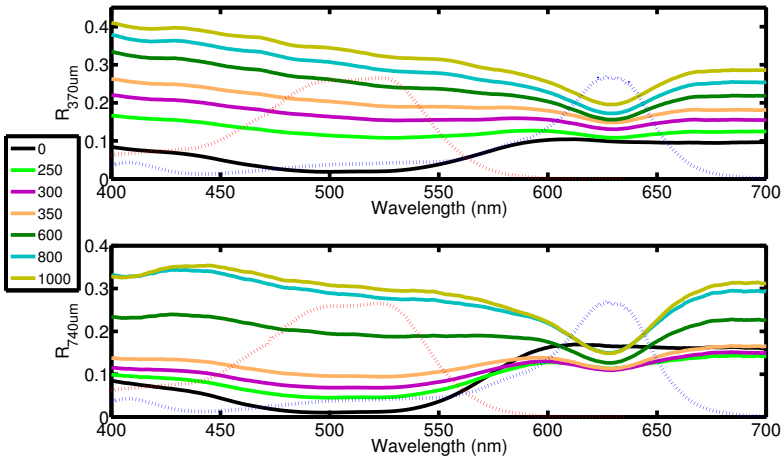


Figure 3.6: Measured reflectance spectra at selected heights for phantom 8. Top and bottom plots correspond to 370 and 740 μm source-detector separations, respectively. Scaled absorbance profiles of red (dashed red line) and blue (dashed blue line) dyes are also included for reference.

number of phantoms, and $x_i(Z_0)$ and $\hat{x}_i(Z_0)$ are the predicted and known values, respectively, at a particular top layer thickness, and $x_{i,max} - x_{i,min}$ is the range of known measurements for variable $x_i$.

The results from these calculations are plotted in Figure 4.3 for the four variables of interest. Overall, amongst the four variables, we see the best agreement in $Z_0$ for which the average NRMSD (for all thicknesses) is 17%. However, as the Figure 4.3 shows, the prediction of the top layer thickness is considerably better for thicknesses up to 550 μm, with an average error of 10%. We see that the error in both the top and bottom layer absorption is also thickness dependent. With increasing top layer thickness, the top layer absorption error decreases while the bottom layer error decreases. Such a result

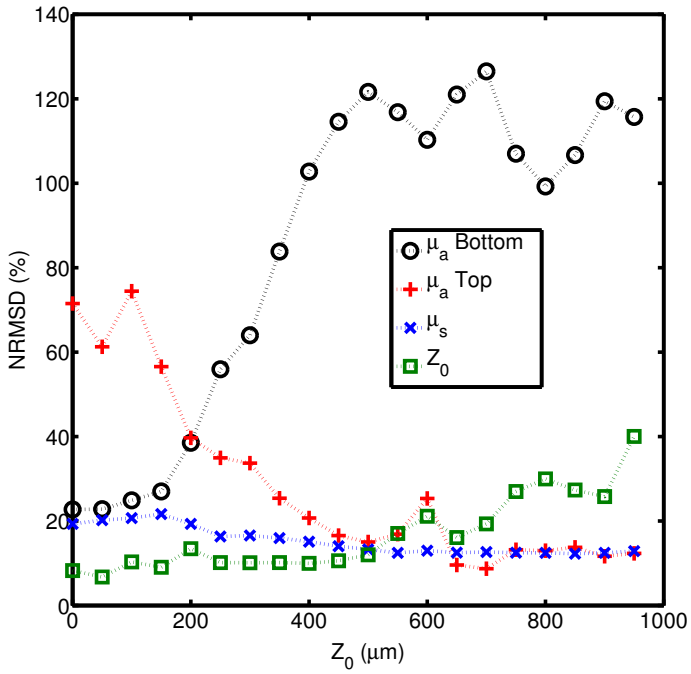


Figure 3.7: Average calculated NRMSD values for each top layer thickness.

is expected as an increasing top layer thickness corresponds to less photons from the bottom layer being measured (and more top layer photons being measured). Therefore, the accuracy of the model prediction to be dependent on $Z_0$. The top layer absorption value decreases from 72% at flush to 12% for $Z_0 = 950$ µm. $\mu_{a,b,max}$ varies from a minimum of 22% at flush up to 118% at maximum thickness. Lastly, the model retains very good accuracy for reduced scattering at 630 nm as the average error (across all thicknesses) is 15%.

The comparison between the measured and expected top layer thicknesses is plotted in Fig. 3.8. The solid line represents perfect agreement. For

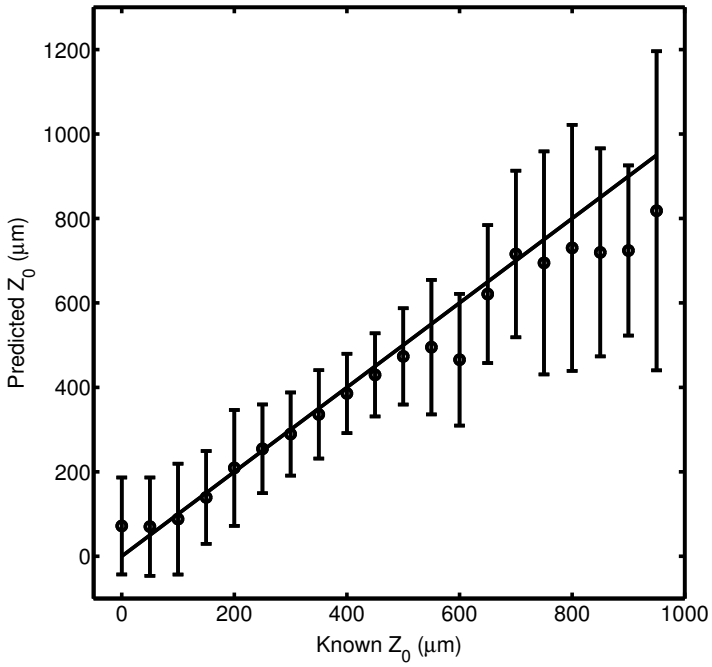


Figure 3.8: Comparison between measured and predicted top layer thicknesses. The error bars in the figure represent the standard deviation of the thickness prediction at each particular height. The solid line is the line of perfect agreement.

$Z_0$ between 100-500 μm the agreement is excellent. As the thickness increases, this agreement decreases and considerable divergence occurs for $Z_0 > 800$ μm. Such a trend is physically expected as the model requires a sufficient number of photons originating from the bottom layer for an accurate prediction; however, the probability of a photon arriving from the bottom layer through a thick top layer is very low, and therefore, the prediction significantly suffers.

To demonstrate how the use of two SDSs improves results, the top layer thickness was also estimated using only one SDS. For an SDS of 370 μm, the

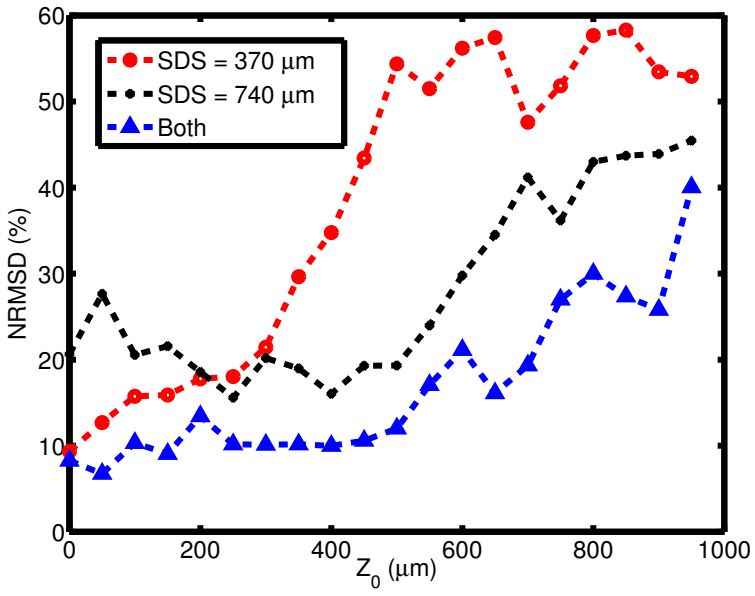


Figure 3.9: NRMSD for $Z_0$ vs. known $Z_0$ for when only one of the SDSs is used and for when both are used. This plot shows how using multiple SDSs can expand the range where $Z_0$ can accurately be predicted.

average error across all thicknesses was 38% with the error increasing rapidly when $Z_0$ was above 300 µm. For an SDS of 740 µm, the average error across all thicknesses was 28%, with increased error relative to the 370 µm detector when $Z_0$ was below 200 µm. The use of multiple SDSs increases the range where $Z_0$ can accurately be predicted. Fig. 3.9 shows the NRMSD for predicted $Z_0$ vs. known $Z_0$ when only one of the SDSs was used. For comparison purposes, the results from using both SDSs are also plotted. Scattering and absorption values were predicted with similar accuracy to using both SDSs.

## 3.7 Conclusions

We present a two-layer Monte Carlo model for skin applications which offers increased utility compared to existing two-layer models as prior knowledge of the top layer thickness is not required. Additionally, our model is sufficiently generalized to be used for a wide variety of probe geometries. The performance of the model has been validated against experimental measurement of reflectance spectra obtained from two-layered liquid phantoms. The phantoms were chosen to span the physiological range of optical properties and three different absorption media (2 food dyes and hemoglobin) were used. In order to construct the depth profiles, spectra were obtained at 50 μm increments until no further changes in spectral profiles occurred. At each height, spectra were measured at two source-detector separations: 370 and 740 μm. We show that the use of multiple SDSs increases the range of values where we can accurately predict top layer thickness. Model predictions of top layer thickness, top and bottom layer absorption coefficient, and reduced scattering coefficient were compared to known experimental values. For thicknesses between 0-550 μm, good agreement was obtained between the numerical and experimental results for top layer thickness and reduced scattering coefficients. The accuracy of top and bottom layer absorption coefficient measurements was found to be highly dependent on top layer thickness, which agrees with physical expectation; however, within appropriate thickness ranges, the error for absorption properties varies from 12-25%. Choosing different source detector separations or including more than two detectors would help to minimize the

dependency of the accuracy on top layer thickness. Based upon these results, our two-layered Monte Carlo lookup table based model shows considerable promise for extracting top layer thicknesses using multiple source-detector diffuse reflectance measurements. In the next chapter, we explore the full potential of our two layer model by performing computational parametric studies to optimize source-detector separation selection for experimental measurement based upon prescribed layer optical properties.

# Chapter 4

# Sampling Depth of Diffuse Reflectance Spectroscopy Probes

This chapter is modified from "Effect of probe geometry and optical properties on the sampling depth for diffuse reflectance spectroscopy" published in The Journal of Biomedical Optics, 2014[1] [12].

## 4.1 Background

Diffuse reflectance spectroscopy (DRS) can be used to noninvasively measure tissue optical properties [6, 10, 11, 14–17, 25, 43–45]. Typically, DRS uses a fiber to inject light into the tissue. The light undergoes scattering and absorption, and the reflected light is collected by a second fiber at a short distance, known as the source-detector separation (SDS), from the illumination fiber. The collected light contains quantitative information which can be extracted using an inverse model that relates the collected signal to tissue optical properties [10, 11]. Since the reflected light only contains information about

[1] **R. Hennessy**, W. Goth, M. Sharma, M.K. Markey, & J.W. Tunnell, "Effect of Source-Detector Separation and Optical Properties on the Sampling Depth for Diffuse Reflectance Spectroscopy Probes." Journal of Biomedical Optics, 19(10), 107002 (October 2014). R. Hennessy developed the computational model. W. Goth and M. Sharma performed the experimental work. M.K. Markey and J.W. Tunnell were advisors.

the tissue that it passes through, accurate interpretation of the results requires knowledge of the penetration depth. The light penetration depth depends not only on the absorption and scattering properties of the tissue, but also on the geometry of the diffuse reflectance probe [46]. Because of this, the sampling depth of a DRS probe can be tune by adjusting the probe geometry, allowing for the design of application specific probes [47].

Many studies have investigated the sampling depth in scattering media both experimentally and numerically [46–50]. Most of these studies rely on the diffusion approximation, which is not valid for short SDSs and highly absorbing media. Others investigated the sampling depth only for reflectance probes with specific geometries, such as single-fiber reflectance [50], overlapping illumination and collection areas [51, 52], large SDSs (SDS $> 1/\mu_s'$) [53], and diffuse reflectance spectroscopy probes only at specific SDSs and fiber diameters [47, 54]. Backman and Gomes recently developed an empirical model to describe sampling depth for a DRS probe. This model is based on a previous study on the sampling depth of single-fiber spectroscopy probes and is only valid for DRS probes with fiber diameters of 200 μm and an SDS of 250 μm [47]. A model that can accurately determine sampling depth for any given SDSs and tissue optical properties will allow the development of application specific probes where light sampling from a specific depth is necessary. Additionally, knowledge of the sampling depth can be used to determine wavelength-dependent differences in the sampling depth due to the difference in optical properties across wavelengths.

In this paper, we analyze the effect of probe geometry and optical properties on the sampling depth using both computational and experimental approaches. First, many Monte Carlo (MC) simulations are performed to determine the sampling depth for a range of optical properties and SDSs. Next, the MC results are validated using a set of phantom experiments. Finally, we developed an analytical expression that can be used to quickly determine the sampling depth for a given SDS, absorption coefficient, and reduced scattering coefficient.

## 4.2 Monte Carlo Model of Sampling Depth

This study adapts the MC model of light transport in layered tissue code developed by Wang et al. [9] implemented in parallel on a GPU using NVIDIA's compute unified device architecture (CUDA) by Alerstam et al [22, 55]. The MC model for modeling light transport is a stochastic method that simulates light transport in a scattering medium with the probabilities of scattering and absorption events determine by the user-specified optical properties of the medium and the geometry of the light source and measurement probe. Photon's step sizes were selected from an exponential distribution that depended on the scattering coefficient, and scattering angles were determined by the scattering anisotropy ($g$) and the phase function. We used the Heyney-Greenstein phase function. Reflection and refraction due to index of refraction mismatches were calculated using the Frensel equation and Snell's law.

A two-layer model was used with reduced scattering in the bottom layer

set to zero, and the absorption in the bottom layer set to $1 \times 10^{15}$ cm$^{-1}$ so that photons reaching the bottom layer were terminated. Scattering anisotropy was held constant at 0.85. The sensitivity of photon path length and sampling depth to phase function and anisotropy ($g$) has been explored by Kanick et al. for single-fiber spectroscopy [50]. They performed simulations with $g = [0.8, 0.9, 0.95]$ and with both the Henyey-Greenstein phase function and the modified Henyey-Greenstein phase function. The data showed that the path lengths and sampling depths are independent of anisotropy. The phase function was found to have an observable effect on path length, but the mean sampling depth remained relatively unchanged.

The refractive index above the medium was set to 1.452 to match the refractive index of an optical fiber, and the refractive index of the medium was set to 1.33 to match the refractive index of water. The top layer absorption coefficient ($\mu_a$) ranged from 0 to 30 cm$^{-1}$ in 20 increments, the top layer reduced scattering coefficient ($\mu_s'$) ranged from 0 to 30 cm$^{-1}$ in 20 increments, and top top layer thickness ($Z_0$) ranged from 0 to 3000 μm in 250 increments. This gave a total of 100,000 separate MC simulations with each using $10^7$ photons. The geometry for the simulations is shown in Figure 4.1(a). Spatially resolved reflectance was calculated by convolving the impulse response using a Gaussian-shaped beam profile with radius $R_1$, and the reflectance signal was calculated by summing the reflectance values centered at the SDS with a collection fiber radius of $R_2$. For a given set of optical properties ($\mu_a$ and $\mu_s'$) and probe geometry parameters (SDS, $R_1$, and $R_2$), we plotted the percentage

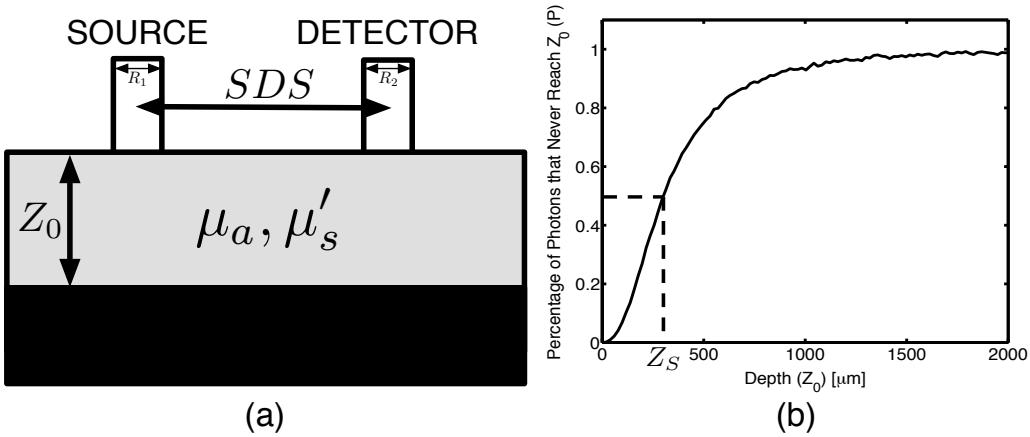


Figure 4.1: (a) A two-layer geometry was used for the Monte Carlo (MC) simulations. The bottom layer had an absorption coefficient of $1 \times 10^{15}$ cm$^{-1}$ and a scattering coefficient of zero so that photons reaching the bottom layer were terminated. The top layer thickness ($Z_0$) ranged from 0 to 3000 μm in 250 increments, the top layer absorption coefficient ($\mu_a$) ranged from 0 to 30 cm$^{-1}$ in 20 increments, and the top layer reduced scattering coefficient ($\mu_s'$) ranged from 0 to 30 cm$^{-1}$ in 20 increments. Reflectance measurements were recorded out to 1 cm from the source. (b) A plot showing the percentage of photons that never reach a depth of $Z_0$ verses $Z_0$ with SDS = 300 μm, $R_1 = 100$μm, $R_2 = 100$μm, $\mu_a = 1.6$cm$^{-1}$, and $\mu_s' = 16$cm$^{-1}$. Sampling depth ($Z_S$) is defined as the depth reached by 50% of the photons.

of photons that never reach depth $Z_0$ versus $Z_0$ (P) in Figure 4.1(b). If we model the curve in Figure 4.1(b) as a sigmoid function, the greatest slope will occur at the depth that is reached by 50% of the photons, meaning that the measured reflectance signal is most sensitive to optical properties at that depth. Because of this, the sampling depth ($Z_S$) of a probe for a given set of optical properties is defined as the depth reached by 50% of the photons.

## 4.3 Experimental Measurements of Sampling Depth

To validate the computational results, 12 different phantoms were constructed in order to perform an experimental analysis of sampling depth for DRS probes of varying SDSs. The phantoms were composed of 5 mL solutions of water, India ink (Salis International, Golden, Colorado, USA), and scattering microbeads (Polysciences, Warrington, Pennsylvania, USA), which spanned absorption and scattering values across a range consistent with those normally found in human tissue. Mie theory was used to determine the scattering properties of the 0.99 μm diameter beads. Mix ratios of water and microbeads were determined so that so that three different scattering spectra from 11 to 25 $cm^{-1}$ were achieved at the reference wavelength of 630 nm. Each of these mix ratios was prepared with four different concentrations of India ink so that the absorption coefficient for the samples ranged from 0 to 23 $cm^{-1}$, results in 12 total phantoms with different scattering and absorption properties, as seen in Table 4.1.

Each of these 12 phantoms was placed into a blackened beaker. Reflection measurements were taken while varying the distance between the probe and the bottom of the beaker from 0 to 3 mm in 50 μm increments. Reflectance spectra were collected at wavelengths from 500 to 700 nm and at SDS of 370, 740, and 1100 μm. Using the known wavelength dependent of scattering and absorption, $\mu_a$ and $\mu_s'$ were calculated at each wavelength, and for each set of $\mu_a$ and $\mu_s'$ a plot of P versus $Z_0$ was created. These plots were then used to calcite $Z_S$ for each set of optical properties.

Table 4.1: Optical properties of phantoms used in sampling depth experiments.

| Phantom | $\mu_s'(\lambda = 630$ nm) | [ink] (% vol.) |
|---|---|---|
| 1 | 11 | 0.00 |
| 2 | 11 | 0.15 |
| 3 | 11 | 0.27 |
| 4 | 11 | 0.45 |
| 5 | 17 | 0.00 |
| 6 | 17 | 0.15 |
| 7 | 17 | 0.27 |
| 8 | 17 | 0.45 |
| 9 | 25 | 0.00 |
| 10 | 25 | 0.15 |
| 11 | 25 | 0.27 |
| 12 | 25 | 0.45 |

## 4.4 Mathematical Model of Sampling Depth

The sampling depth for a DRS probe is dependent on the optical properties ($\mu_a$ and $\mu_s'$) and the probe geometry parameters (SDS, $R_1$, and $R_2$). The sampling depth data from the MC simulations were accurately described by the equation

$$Z_S = a_1 + a_2 \left( \frac{1}{(1 + a_3 \mu_a)^{a_4}} \right) \left( \frac{1}{(1 + a_3 \mu_s')^{a_4}} \right). \tag{4.1}$$

Equation 4.1 is an empirical expression that accurately describes the MC sampling depth data. This expression was found by trying thousands of candidate function with help of TableCurve 2-D (Automated Curve Fitting and Equation Discovery Software, Systat, 2002). Equation 4.1 has four free parameters $(a_1, a_2, a_3, a_4)$ whose values must be determined by first fitting the MC data.

This was accomplished by minimizing the residual between the MC sampling depth results and the sampling depths calculated using Equation 4.1 and a Levenberg-Marquardt algorithm scripted in MATLAB. The dependence of the free parameters on SDS was then determined so that Equation 4.1 could be used to determine sampling depth for a given probe geometry and set of optical properties. SDS and $Z_S$ are in units of cm, and $\mu_a$ and $\mu_s'$ are in units of $\text{cm}^{-1}$.

## 4.5 Results

### 4.5.1 Experimental Validation

The sampling depth results from the phantom experiments were used to validate the computational sampling depth results at SDSs of 370, 740, and 1100 μm with optical properties in the range $\mu_a \in [0 - 25]$ $\text{cm}^{-1}$, and $\mu_s' \in [0 - 30]$ $\text{cm}^{-1}$. Figures 4.2(a-c) plot $Z_S$ predicted by the MC model vs. experimental values for $Z_S$ and show excellent agreement. Figures 4.2(d-f) show an overlay of the computational (transparent mesh) and the experimental (colored surface) results and provides a visual illustration of the good agreement between the experimental and computational results. The room-mean-squared percent error for an SDS of 370 μm was 1.71%, for an SDS of 710 μm it was 1.27%, and for 1100 μm it was 1.24%. This agreement indicates that the MC model accurately models sampling depth. The ripples in the data indicate that the agreement between the phantom measurements and the MC data is wavelength dependent. We believe this is due to the use of the inverse

Table 4.2: Values for fitting parameters at various fiber diameters.

| Diameter (μm) | $a_1$ | $a_2$ | $a_3$ | $a_4$ |
|---|---|---|---|---|
| 50 | 0.187SDS | 1.87SDS + .004 | $(2.80\text{SDS} + .16)^2$ | 0.85 |
| 100 | 0.186SDS | 1.83SDS + .01 | $(2.55\text{SDS} + .18)^2$ | 0.85 |
| 200 | 0.183SDS | 1.81SDS + .013 | $(2.31\text{SDS} + .19)^2$ | 0.85 |
| 400 | 0.175SDS | 1.78SDS + .015 | $(1.87\text{SDS} + .22)^2$ | 0.85 |

power law to describe the wavelength dependence of scattering in the phantoms containing polystyrene microbeads, which in reality, the true scattering values of the phantoms as a function of wavelength contain "humps" in the curve due to the relatively narrow size distribution of the microspheres.

### 4.5.2 Analytical Model of Sampling Depth

The analytical model of sampling depth shown in Equation 4.1 was fit to MC data for a probe with fiber diameters of 50, 100, 200, and 400 μm. For each fiber diameter, SDS ranges from adjacent fiber up to 1000 μm, $\mu_s'$ ranges from 3 to 40 $\text{cm}^{-1}$, and $\mu_a$ ranges from 0 to 40 $\text{cm}^{-1}$. Fitting parameters $a_1$ and $a_2$ were found to have a linear relationship with SDS, $a_3$ was found to have a quadratic relationship with SDS, and $a_4$ is a constant. Table 4.2 shows the fitting parameters used for the four different fiber diameters as a function of SDS. Table 4.2 allows the fitting parameters in Equation 4.1 to be determined for a given fiber diameter and SDS so that Equation 4.1 can be used to determine sampling depth for a specific probe geometry.

Figure 4.3 below shows the sampling depth predicted by the analytical model in Equation 4.1 and Table 4.2 versus the MC sampling depth. Model

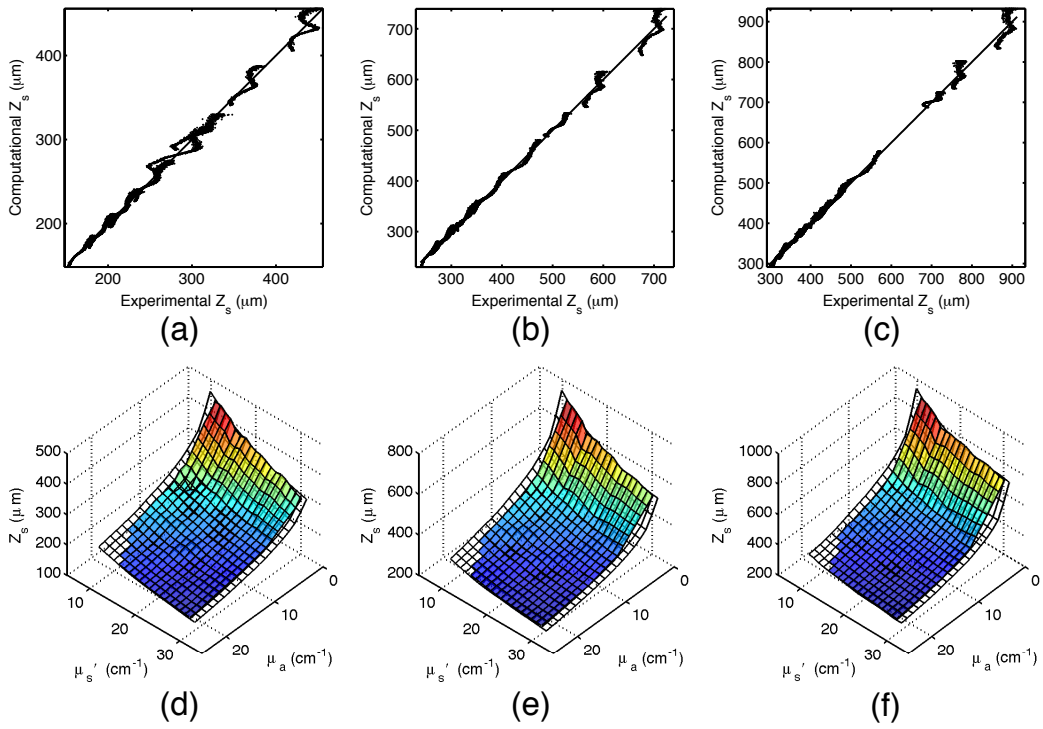


Figure 4.2: Plots of $Z_S$ predicted by Monte Carlo modeling versus the experimental values of $Z_S$ at source-detector separations (SDS) of (a) 370, (b) 740, and (c) 1100 μm. An overlay of two-dimensional surfaces showing the relationship between scattering and absorption on sampling depth for both Monte Carlo and experimental results. These plots provide a visual illustration of the agreement between the computational (transparent mesh) and experimental (colored surface) results for source-detector separations (SDS) of (d) 370, (e) 740, and (f) 1100 μm.

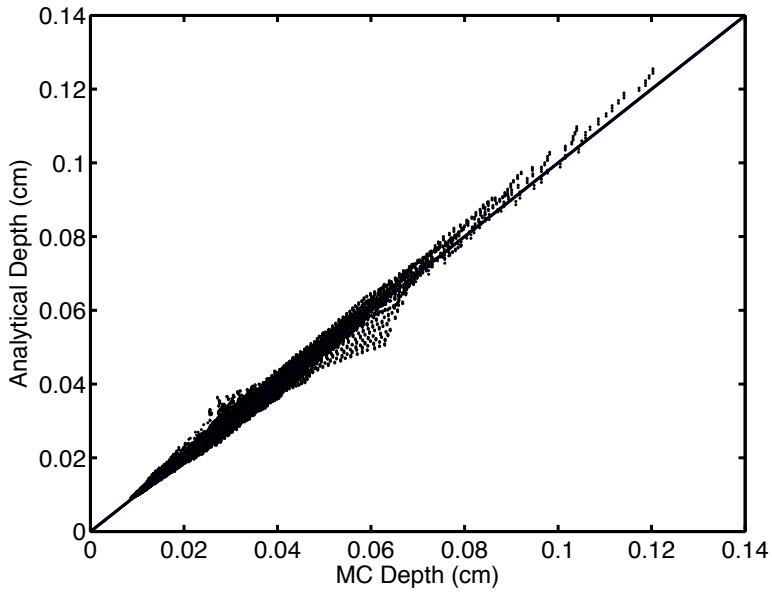


Figure 4.3: Monte Carlo results for simulation of sampling depth versus sampling depth prediction from the analytical model for all four fiber diameters [Equation 4.1]. The line of unity is shown for comparative purposes. There is a 2.89% error between the Monte Carlo simulation results and the analytical model results.

predictions were strongly correlated with the MC data with a mean residual error of 2.89%.

### 4.5.3 Effect of Anisotropy and Phase Function of Sampling Depth

Because scattering anisotropy and the choice of a phase function can impact reflectance at short SDSs [56], a subset of MC simulations was performed to investigate the effect of anisotropy and phase function on sampling depth. The data showed no change in sampling depth for simulations of different anisotropy values ($g = [0.80, 0.85, 0.90, 0.95]$) over a range of optical

properties ($\mu_a \in [0-25]$ cm$^{-1}$, $\mu_s' \in [0-30]$ cm$^{-1}$) and probe geometries (SDS $\in [50-800]\mu$m, $R \in [50-400]\mu$m). This is illustrated in Figure 4.4(a), where sampling depth vs. SDS is plotted for a probe with 50 μm diameter fibers, a reduced scattering coefficient of 10 cm$^{-1}$ and an absorption coefficient of 10 cm$^{-1}$ for four different anisotropy values. The mean percent error across all anisotropy values for all probe geometries and optical properties was 3.74%. Additionally, the eta shows no change in sampling depth for simulations performed with the Heyney-Greenstein (HG) phase function or the modified Heyney-Greenstein (MHG) phase function. This is illustrated in Figure 4.4(b), where the sampling depth versus SDS is plotted for a probe with 50 μm diameter fibers, and anisotropy values of 0.85, a reduced scattering coefficient or 10 cm$^{-1}$, and an absorption coefficient of 10 cm$^{-1}$ for both the HG and MHG phase function. A change in g or the phase function did affect the raw reflectance values; however, there was no change in the sampling depth as defined in this study. These results agree with the findings by Kanick et al. for single-fiber reflectance spectroscopy that show sampling depth is unaffected by both the anisotropy value and the choice of phase function [50].

## 4.6 Discussion and Conclusions

This study utilizes an MC model to investigate how the optical properties of a turbid media and the geometry of a DRS probe affect sampling depth. This MC model for sampling depth was experimentally validated and was shown to accurately predict sampling depth. We developed an analytical

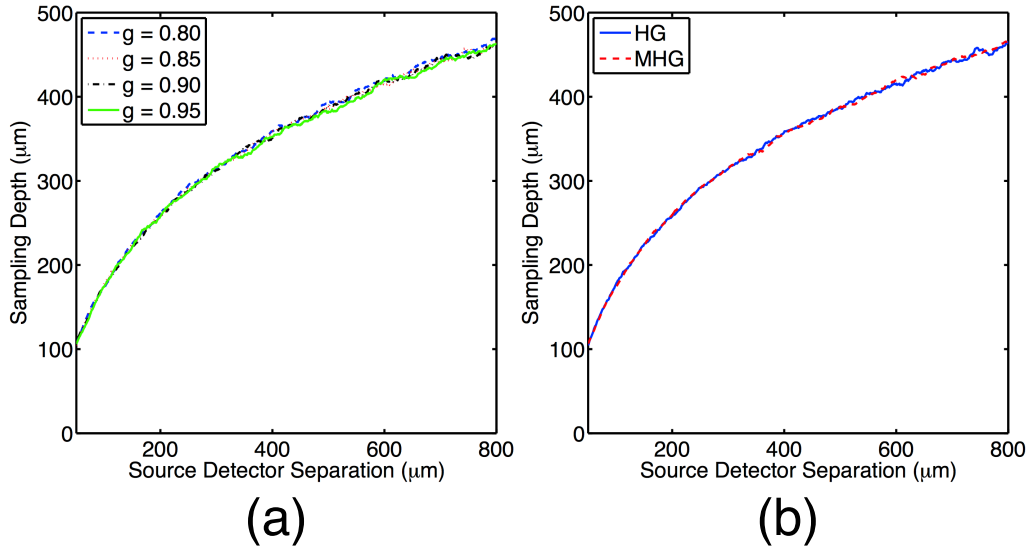


Figure 4.4: (a) Sampling depth versus SDS for varying anisotropy values with $\mu_a = 10$ cm$^{-1}$, $\mu_s' = 10$ cm$^{-1}$, and fiber diameter at 50 μm. (b) Sampling depth versus SDS for both HG and MHG phase functions with $\mu_a = 10$ cm$^{-1}$, $\mu_s' = 10$ cm$^{-1}$, $g = 0.85$ and the fiber diameter at 50 μm.

model where sampling depth is expressed in terms of optical properties and probe geometry.

The utility of the model prediction of sampling depth is shown in Figure 4.5, which plots sampling depth versus fiber diameter for a probe geometry where the source and detector fibers are adjacent for multiple combinations of optical properties. Figure 4.5 was created using MC simulations and not the empirical model in Equation 4.1. This type of probe geometry accurately models the commonly used 6-around-1 fiber orientation, where a center fiber is used for illumination and six collection fiber of the same size are placed around the illumination fiber. All three series have the same value for scattering ($\mu_s' = 10$ cm$^{-1}$), and series 1 represents a moderately absorbing tissue ($\mu_a = 10$ cm$^{-1}$, series 2 represents a highly absorbing tissue ($\mu_a = 20$ cm$^{-1}$, and series 3 represents a non-absorbing tissue ($\mu_a = 0$ cm$^{-1}$). As expected, the sampling depth decreases with increasing absorption. Importantly, a relatively small increase in sampling depth results from a large change in fiber diameter. This is especially evident in the highly absorbing tissue. For example, in series 3, doubling the fiber diameter from 500 to 1000 μm only increases the sampling depth by 17% (from 240 to 270 μm). This result indicates that the 6-around-1 orientation is best for interrogating shallow depths and that it may not be possible to substantially increase sampling depth by increasing the fiber diameter.

The models developed in this study can also be used to provide an estimate of wavelength-dependent differences in optically sampled tissue vol-

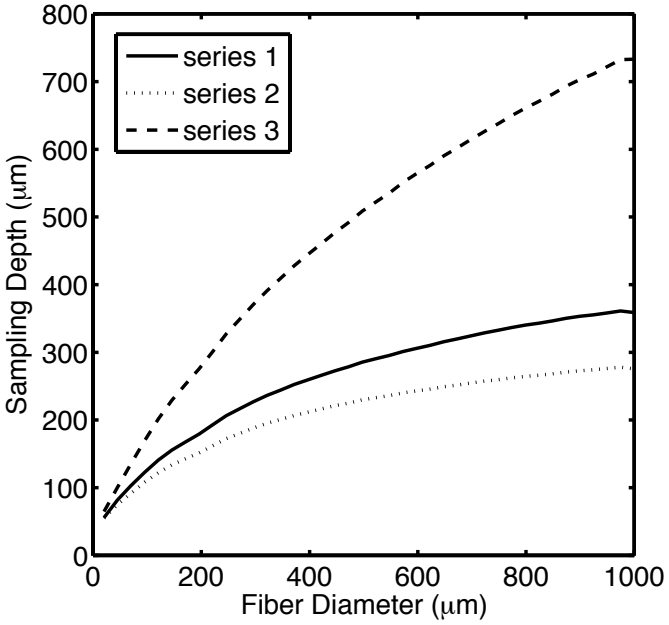


Figure 4.5: Mathematical model estimates of sampling depth for adjacent fibers for three different sets of optical properties: series 1 ($\mu_a = 10$ cm$^{-1}$, $\mu_s' = 10$ cm$^{-1}$), series 2 ($\mu_a = 0$ cm$^{-1}$, $\mu_s' = 10$ cm$^{-1}$), series 3 ($\mu_a = 20$ cm$^{-1}$, $\mu_s' = 10$ cm$^{-1}$). These data were created using MC simulation and not the empirical model in Equation 4.1.

umes, which occurs when optical properties change as a function of wavelength. Figure 4.6 shows sampling depth as a function of wavelength for a sample containing 1 mg/ml of fully oxygenated hemoglobin at three different SDSs. The reduced scattering coefficient is 20 $cm^{-1}$ across all wavelengths. The models can also be used to explain discrepancies between measurements of tissue taken with different probe geometries. The main utility of the proposed model is that it can be used to aid in the design of application specific DRS probes. For example, to design a probe that measures the properties of the epidermis, one may desire a sampling depth equal to or less than the epidermal thickness ( 70 μm [57]) to ensure that most sampled photons only interact with the epidermis and not the dermis. As shown in Figure 4.5, achieving a sampling depth of less than 70 μm would require a 6-around-1 fiber orientation with fibers diameters of 50 μm or less.

This study uses an MC model of DRS to investigate the effect of optical properties and probe geometry on the sampling depth of photons collected by a DRS probe. The MC model of sampling depth was experimentally validated and shown to accurately predict sampling depth. An analytical model of sampling depth was developed and is valid for a DRS probe with fiber diameters of 50, 100, 200, and 400 μm and for a wide range of SDSs (200 to 1000 μm), absorption coefficients (0 to 40 $cm^{-1}$), and reduced scattering coefficients (0 to 40 $cm^{-1}$). The model of sampling depth indicates that for adjacent fibers in the 6-around-1 orientation, the sampling depth cannot be significantly increased by increasing the fiber diameters. This result suggests that deeper

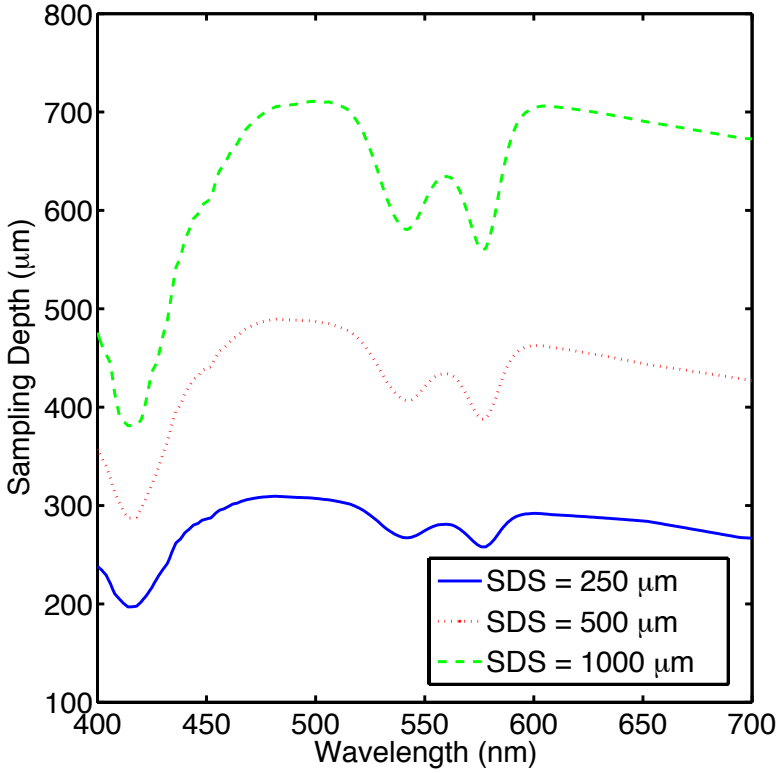


Figure 4.6: Sampling depth versus wavelength for a sample containing 1 mg/ml of fully oxygenated hemoglobin at source detector separations of 250, 500, and 1000 μm. Reduced scattering is 20 $cm^{-}1$ across all wavelengths.

sampling depth can only be accomplished by increasing the gap between the source and collection fibers. Future work will involve the application of the sampling depth model to aid in the design of application specific probes that will be used to interrogate the optical properties of specific layers of tissue such as the epidermis and the dermis. In the next chapter, we show that the one-layer assumption for skin can lead to significant errors in extracted properties.

# Chapter 5

# Impact of the One-Layer Assumption of Diffuse Reflectance Spectroscopy of Skin

This chapter is modified from "Impact of one-layer assumption on diffuse reflectance spectroscopy of skin" published in The Journal of Biomedical Optics, 2015[1] [13].

## 5.1 Background

Diffuse reflectance spectroscopy (DRS) is an optical technique that has been widely used to noninvasively measure skin optical properties [14, 15, 25, 41, 58–62]. Typically, a DRS probe consists of a group of fibers that are placed in contact with the skin. The most common fiber orientation is the six-around-one geometry where a central fiber connected to a light source injects light into the tissue, and the six peripheral fibers collect the light that has travelled through the tissue and returned to the surface. This light contains quantitative information about the tissue that it has passed through, and this information

[1] **R. Hennessy**, M.K. Markey, & J.W. Tunnell, "Errors Caused by One-Layer Assumption of Skin for Diffuse Reflectance Spectroscopy." Journal of Biomedical Optics, 20(2), 028001 (February 2015). R. Hennessy developed the computational model. M.K. Markey and J.W. Tunnell were advisors.

can be used to assess the tissue's physiological state. A model that relates the diffuse reflectance to physiological properties of tissue is used to extract physiological parameters from the DRS spectra. Many models based on the diffusion approximation have been developed to extract properties from DRS spectra; however, this technique requires SDSs of at least 1 mm [6, 14, 63]. Because the thickness of the epidermis is on the order of 100 μm [57], source detector separations (SDS) much less than 1 mm are necessary in order to probe the epidermis properties, meaning the assumptions required for the diffusion approximation are invalid. To overcome this problem, recently developed models for extracting physiological properties from DRS spectra have used Monte Carlo simulations to model the transport of photons through tissue [10, 19, 64]. Most of these models are based on the assumption that skin is homogeneous and that properties are independent of depth. In reality, skin is composed of multiple layers with different properties. For example, melanin is located primarily in the epidermis, whereas hemoglobin is only located in the dermis. Additionally, the thickness of the epidermis varies with anatomical location. Assuming that skin is homogenous can lead to errors in the extracted physiological properties because variations in epidermal thickness can make the measurement of chromophore concentrations difficult by changing the sensitivity of the probe to each layer. Some multilayered inverse models of skin have been developed to overcome this problem [11, 34, 37, 38, 65, 66]. While depth dependent heterogeneities were analyzed in this study, heterogeneities that are spatially in the plane of detection were not considered. Such heterogeneities

would include the border of a nevus or other concentrations of pigment in the skin as well as the localization of hemoglobin in vessels, which was investigated by Fredriksson *et al.* [65]. Additionally, Fredriksson *et al.* generated a spectra using a two layer model of skin with individual blood vessels and fit those spectra with a one layer model. They found that using the one layer model led to much greater errors in extracted parameters when compared to using a three layer model to fit the spectra[65].

In this study, we analyze the specific errors that are caused by the one-layer assumption of skin. This is accomplished by first creating modeled DRS spectra using a two-layered forward diffuse reflectance skin model in the 400 - 750 nm wavelength range with a SDS of 250 μm. Next, parameters are extracted from the spectra using an inverse one-layer, or homogenous, skin model. The extracted parameters can then be compared to the parameters used to generate the modeled two-layer spectra, and this allows for a quantitative and systematic analysis of the errors that arise from the homogeneity assumption for skin.

## 5.2 Two-Layer Forward Model

Modeled spectra were created using a two-layer skin model based on a Monte Carlo lookup table (MCLUT) approach [11]. A four-dimensional MCLUT was created using a two-dimensional Monte Carlo code written in ANSI C [9] implemented on an NVIDIA GTX 560 Ti GPU on 386 parallel threads [55]. The refractive index above the tissue was set to 1.45 to match

the refractive index of an optical fiber, and the refractive index of the medium was set to 1.4 to match the refractive index of tissue. Spatially resolved diffuse reflectance was calculated by convolving the impulse response using a Gaussian shaped beam profile with a radius of 100 μm, and reflectance was calculated at a center-to-center SDS of 250 μm with a 100 μm radius collection fiber [24]. This geometry was chosen because of its common use in skin applications [16]. Each entry in the MCLUT contains a reflectance value for a given top layer thickness ($Z_0$), epidermal absorption ($\mu_{a,epi}$), dermal absorption ($\mu_{a,derm}$), and reduced scattering coefficient ($\mu_s'$), which is assumed to be equal in both layers. In the MCLUT, $Z_0$ ranges from 0 to 1000 μm, $\mu_{a,epi}$ ranges from 0 to 50 cm$^{-1}$, $\mu_{a,derm}$ ranges from 0 to 50 cm$^{-1}$, and $\mu_s'$ ranges from 0 to 70 cm$^{-1}$. Ten evenly spaced increments were used for each of the parameters, giving a total of 10,000 separate MC simulations. A total of $10^7$ photons were used for each MC simulations. The Henyey-Greenstein phase function was used for sampling scattering angles. Scattering anisotropy was set to 0.85 for all simulations.

The MCLUT based forward model for diffuse reflectance is based on a two-layer skin model where a reference absorption spectrum of melanin [67] is used for the top layer and oxy- and deoxy- hemoglobin [68] spectra are used for the bottom layer with a wavelength range of 400 - 750 nm. Spectra are generated by first selecting the following properties: (1) epidermal thickness ($Z_0$), (2) hemoglobin concentration ($[Hb]$), (3) oxygen saturation ($SO_2$), (4) melanin concentration ($[mel]$]), and (5) $\mu_s'(\lambda_0)$. Reduced scattering at all wavelengths is calculated using Equation 5.1, which is commonly used in tissue

optics [10, 11, 19, 64].

$$\mu_s'(\lambda) = \mu_s'(\lambda_0) \times \left(\frac{\lambda}{\lambda_0}\right)^{-B} \tag{5.1}$$

where $\mu_s'$ is the reduced scattering coefficient at wavelength $\lambda$, $\lambda_0 = 630$ nm, and $B$ is the scattering exponent, which is related to the size of the scattering particles. Absorption in the top layer at each wavelength is calculated using Equation 5.2

$$\mu_{a,epi}(\lambda) = \varepsilon_{mel}(\lambda)[mel] \tag{5.2}$$

where $\mu_{a,epi}(\lambda)$ is the epidermal absorption coefficient at wavelength $\lambda$, $\varepsilon_{mel}(\lambda)$ is the extinction coefficient of melanin at wavelength $\lambda$, and $[mel]$ is the concentration of melanin. Absorption in the bottom layer at each wavelength is calculated using Equation 5.3

$$\mu_{a,derm}(\lambda) = [Hb][\varepsilon_{HbO_2}(\lambda)SO_2 + \varepsilon_{Hb}(\lambda)(1 - SO_2)] \tag{5.3}$$

where $\mu_{a,derm}(\lambda)$ is the dermal absorption coefficient at wavelength $\lambda$, $[Hb]$ is the total concentration of hemoglobin, $\varepsilon_{HbO_2}(\lambda)$ is the extinction coefficient of oxygenated hemoglobin at wavelength $\lambda$, $\varepsilon_{Hb}(\lambda)$ is the extinction coefficient of deoxygenated hemoglobin at wavelength $\lambda$, and $SO_2$ is the oxygen saturation. Once the optical properties are determined at each wavelength, the MCLUT is used to determine the reflectance at each wavelength. Cubic splines are used to interpolate between values in the MCLUT.

## 5.3 One-Layer Inverse Model

A one-layer inverse skin model was used to extract the parameters from the two-layer spectra. The same code used to generate the two-layer MCLUT was also used to create the one-layer MCLUT. Refractive indices and probe geometry parameters were also the same. In the one-layer MCLUT, $\mu_s'$ ranges from 0 to 70 cm$^{-1}$ and $\mu_a$ ranges from 0 to 50 cm$^{-1}$ to cover the range of optical properties present in skin [69]. Ten evenly spaced increments were used for each parameter. In the one-layer inverse model, the first step is to set initial values to the following parameters: (1) $\mu_s'(\lambda_0)$, (2) $[mel]$, (3) $[Hb]$, (4) $SO_2$, and (5) vessel radius ($R_{vess}$). Next, $\mu_s'(\lambda)$ is calculated using Equation 1 and $\mu_a(\lambda)$ is determined using Equation 5.4.

$$\mu_a(\lambda) = \varepsilon_{mel}(\lambda)[mel] + \mu_{a,Hb}^{corrected}(\lambda) \tag{5.4}$$

where $[mel]$ represents the concentration of melanin and $\mu_{a,Hb}^{corrected}(\lambda)$ is the wavelength dependent absorption due to hemoglobin that has been corrected for the inhomogeneous distribution. Because hemoglobin is confined to very small volumes in blood vessels, we account for this inhomogeneous distribution in tissue by using the corrections described by van Veen et al. to calculate a corrected absorption coefficient of blood [70]. The correction factor can be calculated using Equation 5.5.

$$C_{pack}(\lambda) = \left[\frac{1 - \exp(-2\mu_{a,bl}(\lambda)r_{vess})}{2\mu_{a,bl}(\lambda)r_{vess}}\right] \tag{5.5}$$

where $\mu_{a,bl}(\lambda)$ is the absorption coefficient of whole blood and $r_{vess}$ is assumed to be the mean vessel radius in the tissue volume sampled. The packaging corrected absorption coefficient of blood in tissue can now be written as shown in Equation 5.6

$$\mu_{a,Hb}^{corrected}(\lambda) = C_{pack}(\lambda)\mu_{a,bl}(\lambda) \tag{5.6}$$

where

$$\mu_{a,bl}(\lambda) = [Hb][\varepsilon_{HbO_2}(\lambda)SO_2 + \varepsilon_{Hb}(\lambda)(1 - SO_2)] \tag{5.7}$$

where $[Hb]$ is the hemoglobin concentration, $\varepsilon_{HbO_2}(\lambda)$ is the extinction coefficient for oxygenated hemoglobin at wavelength $\lambda$, $\varepsilon_{Hb}(\lambda)$ is the extinction coefficient for deoxygenated hemoglobin at wavelength $\lambda$, and $SO_2$ is the oxygen saturation. After Equations 5.1, 5.4, 5.5, 5.6, and 5.7 are used to calculate $\mu_a(\lambda)$ and $\mu_s'(\lambda)$, the one-layer MCLUT is used to generate a reflectance spectrum. The root-mean-sqared error between this spectrum and the modeled two-layer spectrum is then calculated. The parameters are then iteratively updated until the error is minimized. An interior-point nonlinear optimization routine provided in the MATLAB optimization toolbox (Mathworks, Nattick, MA, USA) was used as the optimization algorithm. In order to avoid converging to a local minima, the optimization algorithm was run three time with three different sets of initialization parameters and then we used the solution that gave the smallest error. We are confident that the global minimum was

found because the three different initialization parameters led to very similar solutions.

## 5.4 Results

Spectra based on a two-layer skin model were generated and then parameters from the spectra were extracted using a one-layer inverse skin model. Figure 5.1 shows a representative fit and illustrates the good agreement between the two-layer and one-layer spectra. Because the same scattering value was used for both layers in the two-layer model, the error in extracted scattering values was alway less than 1.7%. Figure 5.2 shows the two-layer $[mel]$ vs. the one-layer extracted $[mel]$. This plot was created by varying the two-layer $[mel]$ used to create the spectra and fixing all other parameters at three different values for $Z_0$ (50 μm, 100 μm, and 200 μm). $[Hb]$ was fixed at 1 mg/ml, $\mu_s'$ was fixed at 20 $cm^{-1}$, $SO_2$ was fixed at 100%, and $B$ was fixed at -1.5. $[mel]$ ranged from 0 to 5 mg/ml in 20 increments. The one-layer inverse model was then used to extract $[mel]$ from each spectra.

Figure 5.3 shows the two-layer $[Hb]$ vs. the one-layer extracted $[Hb]$. This plot was created by varying the two-layer $[Hb]$ used to create the spectra and fixing all other parameters at three different values for $Z_0$ (50 μm, 100 μm, and 200 μm). $[mel]$ was fixed at 1 mg/ml, $\mu_s'$ was fixed at 20 $cm^{-1}$, $SO_2$ was fixed at 100%, and $B$ was fixed at -1.5. $[Hb]$ ranged from 0 to 3 mg/ml in 20 increments. The one-layer inverse model was then used to extract $[Hb]$ from each spectra.

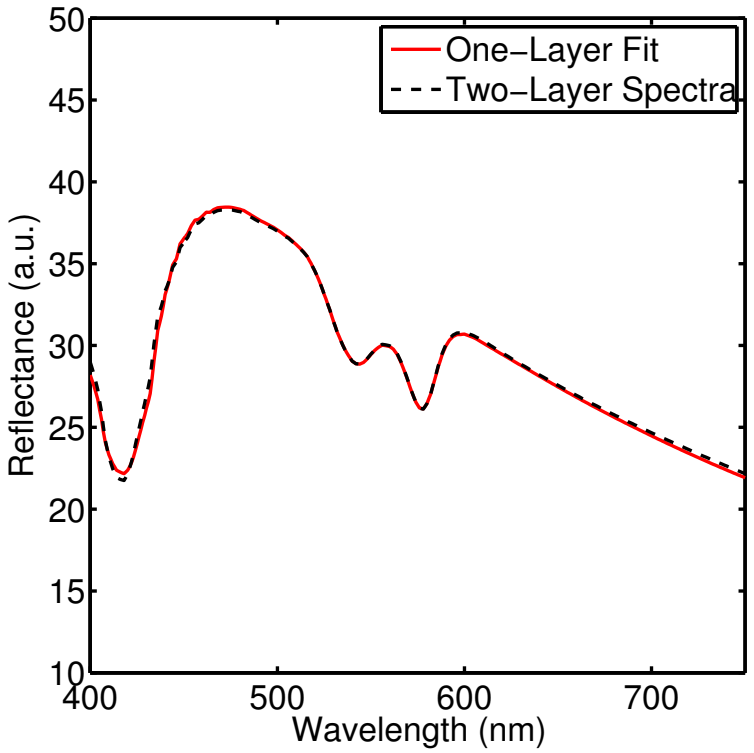


Figure 5.1: A representative fit showing the good agreement between the two-layer and one-layer spectra.

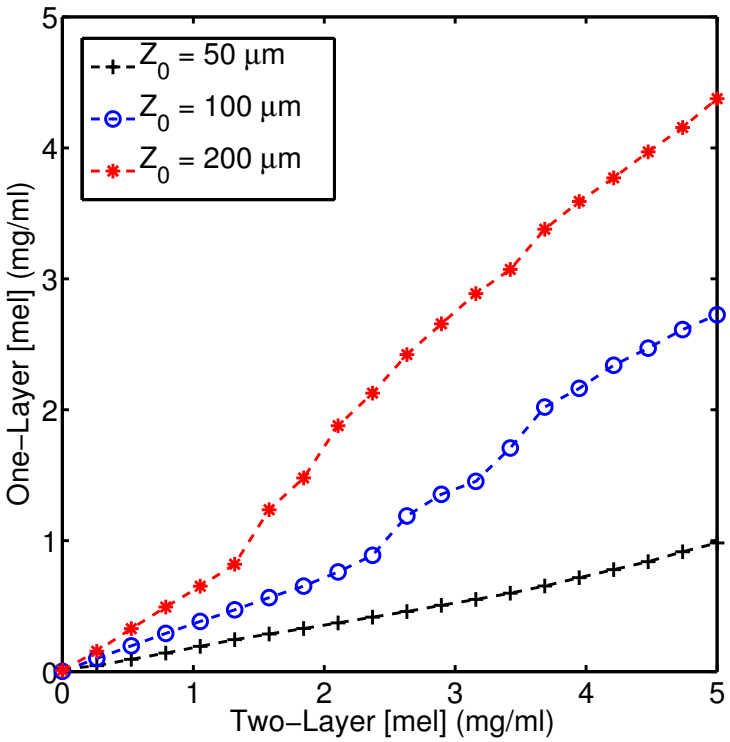


Figure 5.2: Two-layer $[mel]$ vs. the one-layer extracted $[mel]$. This plot was created by varying the two-layer $[mel]$ used to create the spectra and fixing all other parameters at three different values for $Z_0$ (50 µm, 100 µm, and 200 µm). $[Hb]$ was fixed at 1 mg/ml, $\mu_s'$ was fixed at 20 cm$^{-1}$, $SO_2$ was fixed at 100%, and $B$ was fixed at -1.5. $[mel]$ ranged from 0 to 5 mg/ml in 20 increments.

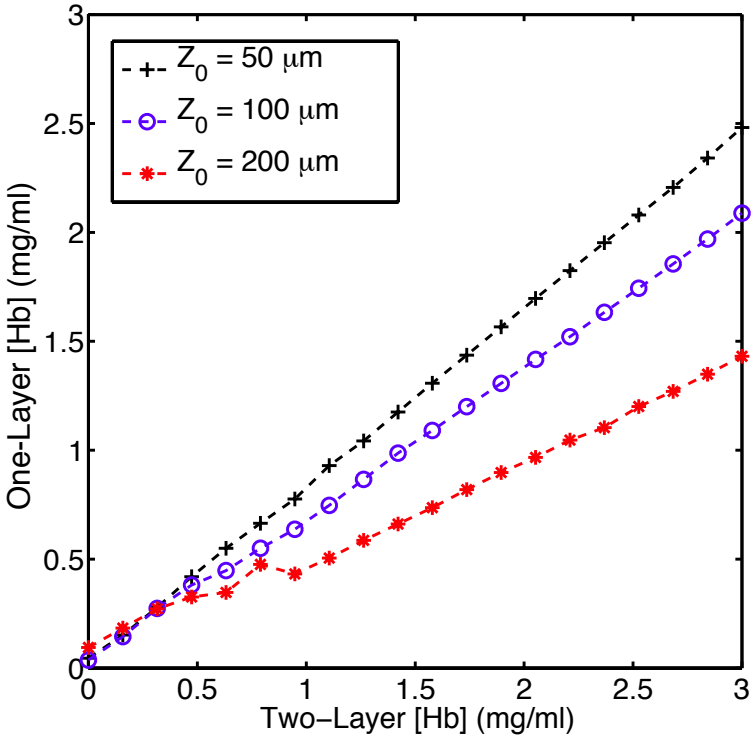


Figure 5.3: Two-layer $[Hb]$ vs. the one-layer extracted $[Hb]$. This plot was created by varying the two-layer $[Hb]$ used to create the spectra and fixing all other parameters at three different values for $Z_0$ (50 $upmu$m, 100 μm, and 200 μm). $[Hb]$ was fixed at 1 mg/ml, $\mu_s'$ was fixed at 20 cm$^{-1}$, $SO_2$ was fixed at 100%, and $B$ was fixed at -1.5. $[mel]$ ranged from 0 to 3 mg/ml in 20 increments.

Figure 5.4 shows the two-layer $SO_2$ vs. the one-layer extracted $SO_2$. This plot was created by varying the two-layer $SO_2$ used to create the spectra and fixing all other parameters at three different values for $Z_0$ (50 μm, 100 μm, and 200 μm). $[mel]$ was fixed at 1 mg/ml, $\mu_s'$ was fixed at 20 $cm^{-1}$, $[Hb]$ was fixed at 1 mg/ml, and $B$ was fixed at -1.5. $SO_2$ ranged from 0 to 100% in 20 increments. The one-layer inverse model was then used to extract $SO_2$ from each spectra.

Figure 5.5 shows $Z_0$ vs. the vessel radius parameter used in the one-layer inverse model. This plot was created by varying $Z_0$ in the two-layer model used to create the spectra and fixing all other parameters. $[mel]$ was fixed at 1 mg/ml, $[Hb]$ was fixed at 1 mg/ml, $\mu_s'$ was fixed at 20 $cm^{-1}$, $SO_2$ was fixed at 100%, and $B$ was fixed at -1.5. $Z_0$ ranged from 0 to 300 μm in 20 increments. The one-layer inverse model was then used to extract vessel radius from each spectra. To illustrate the relationship between the pigment packaging factor in the one-layer model and the epidermal thickness, a pigment packaging factor was not included in the two-layer model.

Figures 5.6(a) and 5.6(b) were created by generating 100 random pairs of $[mel]$ and $[Hb]$ to generate two-layer spectra while all other parameters were fixed. $Z_0$ was fixed at 100 μm, $\mu_s'$ was fixed at 20 $cm^{-1}$, $SO_2$ was fixed at 100%, and $B$ was fixed at -1.5. The random pairs of $[Hb]$ and $[mel]$ used to generate the two-layer spectra are plotted in Figure 6(a) and the extracted one-layer values for $[Hb]$ and $[mel]$ are plotted in Figure 6(b). In Figure 6(a), $[Hb]$ and $[mel]$ have a Pearson correlation coefficient (PCC) of R = 0.0438. In

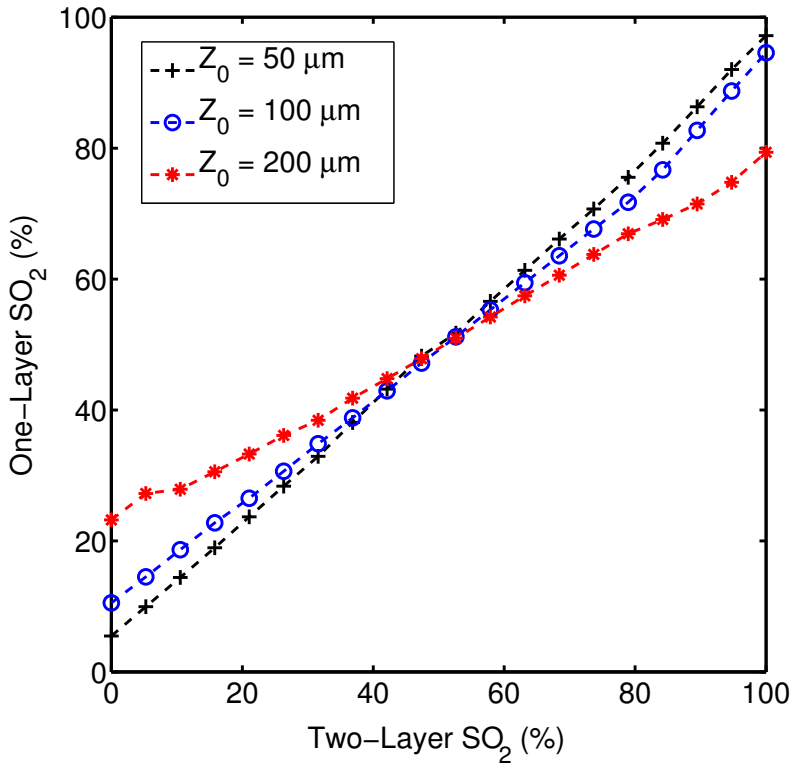


Figure 5.4: Two-layer $SO_2$ vs. the one-layer extracted $SO_2$. This plot was created by varying the two-layer $SO_2$ used to create the spectra and fixing all other parameters at three different values for $Z_0$ (50 µm, 100 µm, and 200 µm). $[mel]$ was fixed at 1 mg/ml, $\mu_s'$ was fixed at 20 $cm^{-1}$, $[Hb]$ was fixed at 1 mg/ml, and $B$ was fixed at -1.5. $SO_2$ ranged from 0 to 100% in 20 increments.

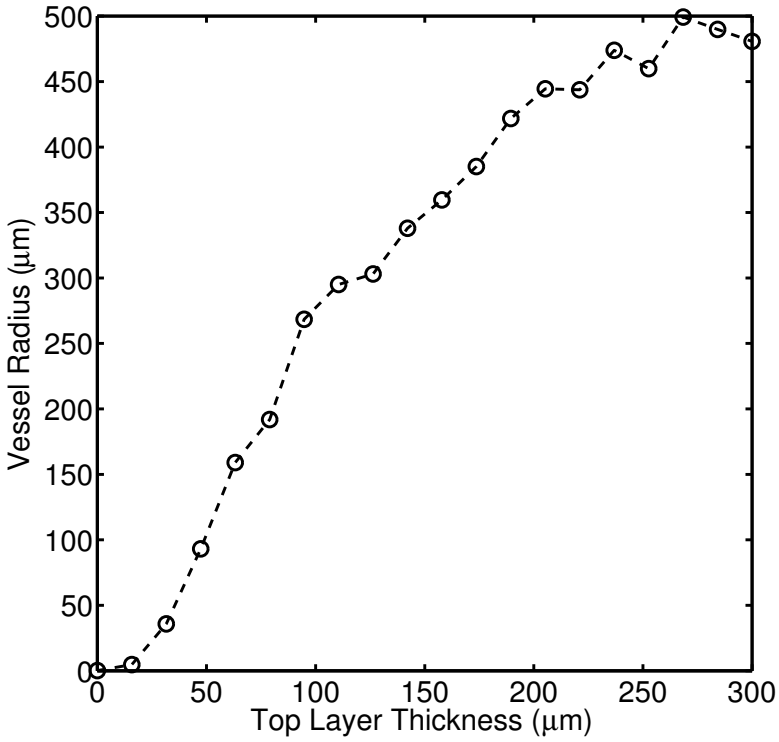


Figure 5.5: $Z_0$ vs. the vessel radius parameter used in the one-layer inverse model. This plot was created by varying $Z_0$ in the two-layer model used to create the spectra and fixing all other parameters. $[mel]$ was fixed at 1 mg/ml, $[Hb]$ was fixed at 1 mg/ml, $\mu_s'$ was fixed at 20 $cm^{-1}$, $SO_2$ was fixed at 100%, and $B$ was fixed at -1.5. $Z_0$ ranged from 0 to 300 µm in 20 increments.

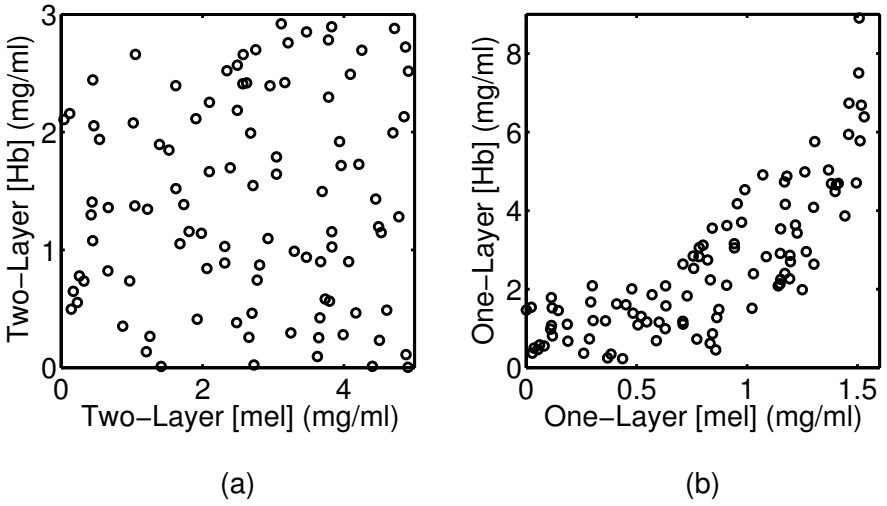


Figure 5.6: (a) Random pairs of $[Hb]$ and $[mel]$ used to generate the two-layer spectra. (b) Extracted one-layer values for $[Hb]$ and $[mel]$.

Figure 6(b), $[Hb]$ and $[mel]$ have a Pearson correlation coefficient (PCC) of R = 0.7950.

## 5.5 Discussion and Conclusions

In this study, we investigated errors caused by using a one-layer assumption for skin when using diffuse reflectance spectroscopy to measure optical properties. This was accomplished by first creating spectra using a two-layer skin model and then extracting the properties from the modeled spectra using a one-layer inverse skin model. The parameters used to generate the two-layer

spectra were then compared to the parameters extracted with the one-layer inverse model.

Figure 5.2 shows the extracted one-layer $[mel]$ vs. the two-layer $[mel]$ for three different epidermal thicknesses. Notice that the one-layer model underestimates $[mel]$; however, this would be expected since the one-layer inverse model is extracting a volume average for $[mel]$, and the melanin is located only in a thin top layer. Additionally, the magnitude of the error is dependent on epidermal thickness, with an underestimation by a factor of 5 when the epidermal thickness is 50 μm and by a factor of approximately 1.25 when the epidermal thickness is 200 μm. If the epidermal thickness is unknown, it would not be possible to interpret a $[mel]$ value extracted with a one-layer skin model. Similarly, Figure 5.3 shows the extracted one-layer $[Hb]$ vs. the two-layer $[Hb]$ for three different epidermal thicknesses. $[Hb]$ is also underestimated when a one-layer skin model is used; however, the errors are smaller than the ones for $[mel]$ and the relationship of the error to epidermal thickness is the opposite with an underestimation of a factor of 1.2 when the epidermal thickness is 50 μm and by a factor of 2 when the epidermal thickness is 200 μm. Figures 5.2 and 5.3 show that $[Hb]$ and $[mel]$ will be underestimated when a one-layer skin model is used and that the magnitude of the underestimation is a function of epidermal thickness. If the epidermal thickness were known, it could be possible to correct for these errors; however, in many clinically realistic scenarios, the epidermal thickness will be unknown. If epidermal thickness could be known *a priori* it would be possible to account

for these errors; however, in most clinically relevant scenarios the epidermal thickness will be unknown.

Figure 5.4 shows the extracted one-layer $SO_2$ vs. the two-layer $SO_2$ for three different epidermal thicknesses. For $SO_2 < 50\%$, the one-layer model overestimates $SO_2$, and for $SO_2 > 50\%$, the one-layer model underestimates $SO_2$. The magnitude of the errors is directly proportional to epidermal thickness, meaning the error will be larger when the epidermis is thicker with error levels reaching 20% when the epidermal thickness is 200 μm. Similar to the problem with using a one-layer model to extract $[mel]$ and $[Hb]$, it will be difficult to interpret $SO_2$ values that are extracted using a one-layer skin model when the epidermal thickness is unknown.

To account for inhomogeneously distributed blood in skin, many one-layer models have incorporated a pigment packaging factor. This factor, often calculated as the average vessel radius, accounts for the flattening of the hemoglobin absorption spectra that is caused by the reduced path length of photons at wavelengths where the absorption is high. We noticed a similar flattening phenomenon is caused by increasing the epidermal thickness. Figure 5.5 was created in order to further investigate the relationship between the vessel radius factor in a one-layer model and the epidermal thickness in a two-layer model. Figure 5.5 shows that there is a strong positive correlation between epidermal thickness and the vessel radius factor. Because of this, we believe the pigment packaging factor is influenced by both the localization of blood in vessels and the localization of blood under the epidermis.

In Figure 5.6, we investigate if the one-layer assumption would have any effect on the correlation between $[mel]$ and $[Hb]$. First, random pairs of $[mel]$ and $[Hb]$ were selected and used to generate two-layer spectra. These random pairs are plotted in Figure 5.6(a) and are essentially uncorrelated with a PCC of R = 0.044. Figure 5.6(b) plots the pairs of $[mel]$ and $[Hb]$ that were extracted using the one-layer model and shows that they are highly correlated with a PCC of R = 0.795. This correlation is due to the wavelength dependence of photon sampling depth. At shorter wavelengths, both scattering and absorption in skin are higher and therefore photons with shorter wavelengths have shallower sampling depths and are more heavily weighted towards the properties of the epidermis [12]. This means that the effect of melanin is larger at shorter wavelengths in a two-layer model. In a one-layer model, this does not occur because hemoglobin and melanin are evenly distributed. When you attempt to fit a one-layer model to two layer data, the one-layer model will underestimate the absorption due to melanin at shorter wavelengths. To compensate for this, the optimization routine can increase the hemoglobin concentration since hemoglobin absorbs strongly at shorter wavelengths. This allows the optimization routine to minimize the error, but causes the artificial correlation between melanin concentration and hemoglobin concentration. We believe that this is the biggest limitation of using a one-layer model since there is no way to correct for the artificial correlation between $[mel]$ and $[Hb]$. Additionally, correlation between extracted parameters can decrease the performance of a classifier. For example, if the extracted parameters were used

to train a classifier for the diagnosis of skin cancer, we would expect inferior performance from the classifier because of the artificial correlation between $[mel]$ and $[Hb]$ that is caused by the one-layer assumption of skin.

We have demonstrated evidence that using a one-layer model for skin to extract properties from DRS spectra leads to errors in the extracted properties. By generating modeled spectra with a more physiologically realistic two-layer model, and then extracting properties from those spectra using a one-layer inverse skin model, we were able to quantitatively and systematically analyze the errors that arise from the one-layer assumption for skin. All of our simulations were performed using a 400-750 nm wavelength range and a SDS of 250 μm since these values are common for DRS in skin. At longer wavelength where the absorption due to hemoglobin and melanin is negligible, a one-layer model could be sufficient. Additionally, a one-layer model could also be sufficient for much larger SDSs where the effect of the epidermis is greatly diminished. The main disadvantage of using a two layer model is the increased computational complexity; however, through the use of a LUT method and advances in GPU computing, this is no longer a major issue. Our results can be used to aid in the interpretation of extracted one-layer parameters, but more importantly, these results provide evidence showing that a one-layer model is inadequate for extracting optical properties from a two-layered tissue. In the next chapter, we use a custom probe to measure take *in vivo* measurements of skin and extract the tissue properties using the two-layer MCLUT model.

# Chapter 6

# *In Vivo* Estimation of Epidermal Thickness, Melanin and Hemoglobin Concentrations, Oxygen Saturation, and Scattering Using Diffuse Reflectance Spectroscopy

## 6.1 Background

Diffuse reflectance spectroscopy (DRS) has been widely used for the noninvasive measurement of tissue properties [2, 3, 71–80]. This technique is able to investigate tissue structure, chromophore concentration, and health by measuring the tissue's optical properties. Typically, a DRS measurement system consists of a broadband light source, a spectrometer, and an arrangement of optical fibers used for delivering and collecting light to and from the tissue. One or more of the optical fibers is connected to the light source and delivers light into the tissue by being placed in direct contact with the tissue. Another set of optical fibers placed in contact at a short distance, called the source-detector separation (SDS), from the illumination fibers collects light that has reflected back to the surface of the tissue and delivers this light to a spectrometer. This collected spectrum is called the diffuse reflectance spectrum and it contains information about the tissue that it has passed through. Extraction of this information from the spectrum requires the use of a computational

model that can relate the collected spectrum to physiological properties. One common approach is to use the diffusion approximation to the radiative transport equation (RTE) [81]; however, this technique requires SDSs on the order of 1 cm [82], and is therefore not practical for use in skin where the epidermal thickness can be less than 100 μm [83]. Another approach involves the use of Monte Carlo simulation to model photon transport in tissue, which can accurately model short SDSs [84]. The major limitation of Monte Carlo simulation is that it's very computationally intensive; however, our recent work has overcome this limitation by using a combination of parallel processing and pre-computed lookup tables [10, 11].

Many techniques for analyzing DRS spectra are based on the assumption that tissue is homogeneous and that properties are independent of depth [6, 10, 14, 85–89]. In reality, most tissue has a layered structure where there is a thin lining of epithelial tissue at the surface. One example of this is skin, where there is a thin epidermal layer on top of the dermal layer [90]. The epidermis contains melanin, whereas the dermis is perfused with blood vessels and nerves [70]. These differences in cellular structure and chemical composition cause the two layers to have very different optical properties. Because of this, assuming that the optical properties in skin are homogenous can lead to significant errors in extracted optical properties. In our previous study (Chapter 5), we were able to show that the homogeneity assumption in skin causes an artificial correlation in hemoglobin and melanin concentrations [13]. Additionally, using a layered model to extract tissue properties provides valuable

information such as epidermal thickness, which can be of great significance in many areas of medical and biological research.

In this study, we used a custom designed DRS probe specifically created for measuring the properties of skin to collect DRS spectra from 80 subjects at 5 different anatomical locations including the cheek, palm, forearm, calf, and back. We then used our previously developed two-layer inverse model for extracting properties from diffuse reflectance spectra in order to measure epidermal thickness, hemoglobin concentration, melanin concentration, scattering properties, and oxygen saturation. The goals of this study are to show that DRS can noninvasively and accurately measure depth epidermal thickness and chromophore concentrations in skin.

## 6.2 Data Collection

### 6.2.1 Study Population

In total, 80 health subjects were included who gave their informed consent for the participation in the study. The study received IRB approval from The University of Texas at Austin (IRB No. 00002030). The study was performed in a university setting (The University of Texas at Austin) during the summer of 2014. We recorded the subjects' age and gender. The average age of participants was 25.7 years and included subjects aged between 18 and 46. There were 51 males and 29 females.

### 6.2.2 Instrumentation

We developed a custom fiber optic DRS probe designed specifically for interrogating the optical properties of skin. Source and detector fiber were arranged so that the photon sampling depth was optimized for measuring the properties of both the epidermis and dermis. This was accomplished by using the work described in chapter 4 [12]. The probe consisted for four separate arms:

1. Central fiber of 40 μm diameter connected to the light source.
2. An inner ring of six 40 μm diameter collection fibers with an SDS of 55 μm connected to the first spectrometer.
3. An outer ring of five 200 μm diameter collection fibers with an SDS of 205 μm connected to the second spectrometer.
4. An outermost ring of fibers that were not used.

The inner ring of 40 μm fibers was designed to sample light that interacts primarily with the epidermis. The outer ring of five 200 μm fibers was designed to sample light that interacts with both the epidermis and the dermis. A diagram of the fiber arrangement is shown in Figure 6.1. The main components of the entire measurement system are a tungsten halogen light source (HL-2000, Ocean Optics, Dunedin, FL, USA) that illuminates between 360-2400 nm, two spectrometers (USB2000+UV-VIS, Ocean Optics,

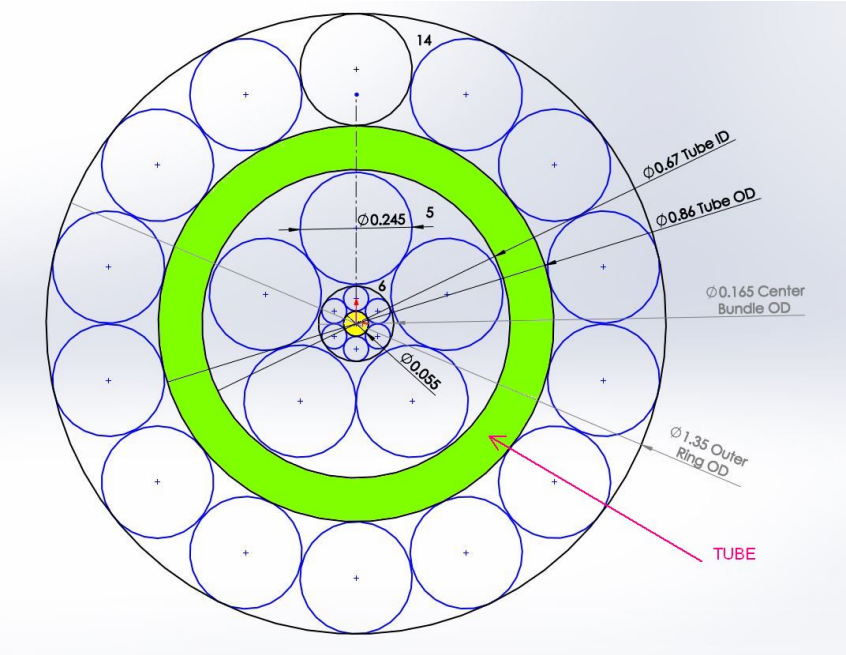


Figure 6.1: Fiber design.

Dunedin, FL, USA), the fiber optic probe described above (FiberTech Optica, Kitchener, Ontario, Canada), and a laptop using OceanView (Ocean Optics, Dunedin, FL, USA) to record the data.

### 6.2.3 *In Vivo* Data Acquisition

Before *in vivo* data were acquired, at the beginning of each day we collected a dark measurement and a calibration measurement using a phantom with known optical properties. The dark measurement was collected by turning lights off in the room and covering the tip of the probe. The calibration measurement was taken by submerging the probe into a calibration phantom with no absorption and a reduced scattering value of 17 $cm^{-1}$ at 630

nm. Reflectance could then be calculated using equation 6.1

$$R(\lambda) = \frac{I_{invivo}(\lambda) - I_{dark}(\lambda)}{I_{cal}(\lambda) - I_{dark}(\lambda)}, \tag{6.1}$$

where $R(\lambda)$ is the reflectance, $I_{invivo}(\lambda)$ is the raw *in vivo* data, $I_{dark}(\lambda)$ is the dark measurement, and $I_{cal}(\lambda)$ is the calibration measurement.

After the dark and calibration measurements, *in vivo* data were collected by placing the probe in direct contact with the subject's skin. Spectra were collected from the forearm, cheek, palm, calf, and lower back. The integration time for both spectrometers was set to 1200 ms. Reflectance values between 425 and 650 nm were saved for processing. Unfortunately, the data from the closest SDS had to be thrown out. We suspect this was caused by an issue with the probe where the inner ring of fibers was obstructed.

## 6.3 Extracting Tissue Properties

Our recently developed Monte Carlo lookup table (MCLUT) for two-layers that was discussed in chapter 3 was used to extract properties from the *in vivo* data. The following properties were extracted from the spectra:

1. Reduced scattering coefficient at 630 nm (assumed to be the same in both layers),
2. The scattering exponent parameter (B),
3. Melanin concentration (confined to the top layer),

4. Hemoglobin concentration (confined to the bottom layer),

5. Oxygen saturation, and

6. Epidermal thickness.

## 6.4 Results and Discussion

Figures 6.2 - 6.7 show the average values of $\mu_s'$, $B$, [mel], [Hb], $SO_2$, and epidermal thickness, respectively, for the five different anatomical locations. The error bars represent the standard deviation of the data. The results were compared to published values of skin properties.

The main goal of the study performed in this chapter was to show DRS can accurately extract depth dependent skin properties *in vivo*. While it's not possible to directly validate the results, we can compare the results to published values for skin optical properties. For reduced scattering (Figure 6.2), we found no significant difference between the 5 different anatomical locations. The average value across all 80 subject for all 5 anatomical locations was $\mu_s'(\lambda = 630 \text{ nm}) = 22.75 \text{ cm}^{-1}$. This result agrees with the review by Lister *et al.* [69] which shows an average reduced scattering value of approximately 20 $\text{cm}^{-1}$ at 630 nm across multiple studies. There was no significant difference found between the 5 anatomical locations for the scattering exponent, $B$ (Figure 6.3).

For melanin concentration (Figure 6.4), we found the measurement from the palm had significantly less melanin when compared to the other

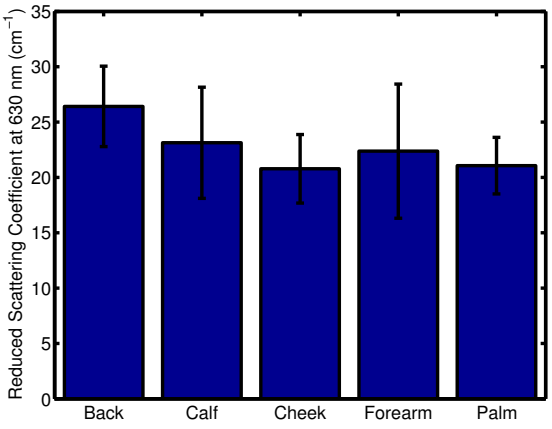


Figure 6.2: Mean and standard deviation of $\mu_s'$ for the N = 80 subjects on their back, calf, cheek, forearm, and palm.

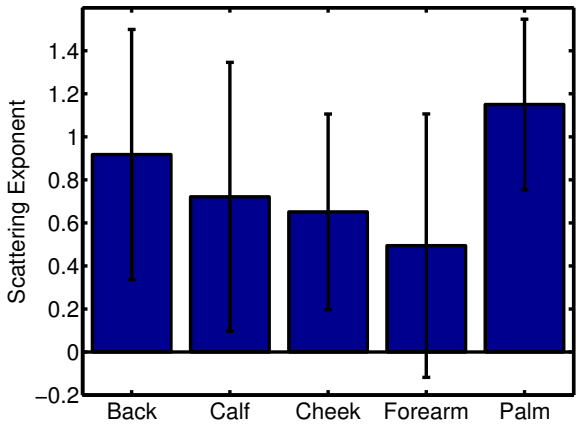


Figure 6.3: Mean and standard deviation of $B$ for the N = 80 subjects on their back, calf, cheek, forearm, and palm.

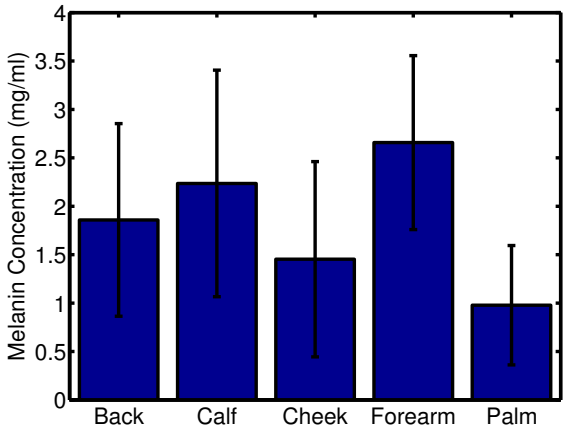


Figure 6.4: Mean and standard deviation of [mel] for the N = 80 subjects on their back, calf, cheek, forearm, and palm.

groups. This result is expected, as skin on the palm is known to have reduced melanin concentration. The average value across all 80 subject for all 5 anatomical locations was [mel] = 1.83 mg/ml in the epidermis. This result agrees with results by Patwardhan *et al.* [91], Marchesini *et al.* [92], and Salomatina *et al.* [93], which all show that 1.83 mg/ml is within the range of normal values for epidermal melanin concentration.

For hemoglobin concentration (Figure 6.5), we found no significant difference between the 5 different anatomical locations. The average value across all 80 subject for all 5 anatomical locations was [Hb] = 1.37 mg/ml in the epidermis. This result agrees with the review by Lister *et al.* [69] which shows a hemoglobin concentration in the dermis of approximately 1.25 mg/ml across multiple studies.

For epidermal thickness (Figure 6.7), we found no significant difference

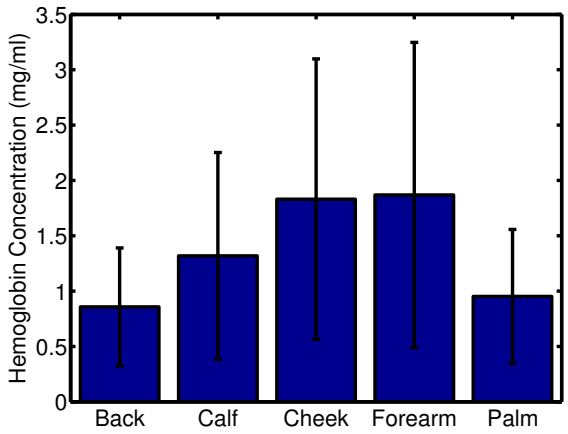


Figure 6.5: Mean and standard deviation of [Hb] for the N = 80 subjects on their back, calf, cheek, forearm, and palm.

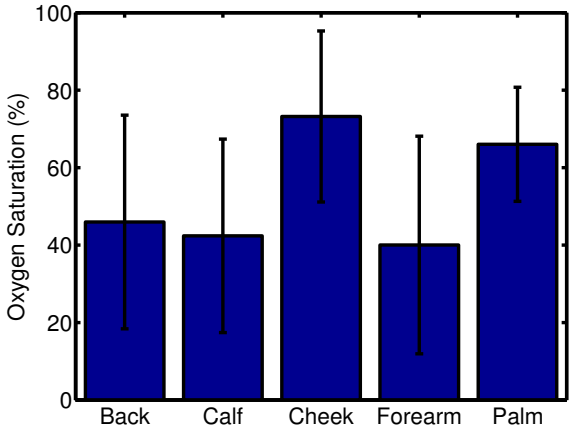


Figure 6.6: Mean and standard deviation of $SO_2$ for the N = 80 subjects on their back, calf, cheek, forearm, and palm.

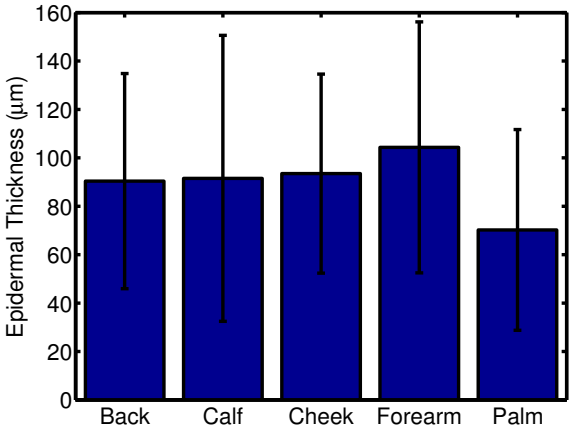


Figure 6.7: Mean and standard deviation of epidermal thickness for the N = 80 subjects on their back, calf, cheek, forearm, and palm.

between the 5 different anatomical locations. This result was unexpected as the palm and lower back are known to have a thicker epidermis, and could be due to short SDS part of the probe not working properly. The average value across all 80 subject for all 5 anatomical locations was 90 μm. This result agrees with the study by Gambichler *et al.* [57] which shows an average epidermal thickness of 75 μm using OCT.

Overall, the results match up well with previously published values for skin properties. This promising finding shows that DRS can be used to measure the depth dependent optical properties of skin *in vivo*. Future work would involve repairing the inner SDS fiber bundle on the probe, collecting more *in vivo* data, and also recording additional information about each subject including skin color or race.

# Chapter 7

# Conclusions

Diffuse reflectance spectroscopy (DRS) is a technology that has high potential for the noninvasive measurement of physiological information. This dissertation extends previously developed methods for analyzing DRS spectra and also develops methods that can be used to optimize the design of DRS instrumentation. We also answered some important questions in the field; for example, what errors arise when a one-layer model of skin is used to analyze DRS spectra, and how DRS instrumentation can be designed to sample light at specific depths.

In Chapter 2, we introduced the Monte Carlo lookup table (MCLUT) method for extracting properties from DRS spectra. Monte Carlo simulation is the most accurate way to model light transport in turbid media; however, its computational intensity has limited its application in inverse models used for extracting properties from DRS spectra. To overcome this issue, we pre-computed reflectance values for a range of optical properties and stored these values in a lookup table (LUT) that could be referred to later on. This allowed for a significant speed up in the inverse model as well as the increased accuracy that came from using Monte Carlo simulation to model light transport.

The MCLUT method was validated using using liquid phantoms made from polystyrene microspheres that scatter light and hemoglobin. Since the concentration of the microspheres and hemoglobin were known, we can compare the known values to the values extracted using the MCLUT method. The results of the validation study showed that the MCLUT method had an error of 1.74% for extracted reduced scattering values and 2.42% for extracted hemoglobin concentration values. These promising results showed that the MCLUT method can be successfully used to extract optical properties from DRS spectra.

In Chapter 3, we extended the MCLUT method described in Chapter 2 to two-layers. This was accomplish by increasing the dimensions of the LUT from just scattering and absorption to scattering, absorption on the top, absorption on the bottom, and the thickness of the top layer. This means that the total number of Monte Carlo simulations increased dramatically, but by performing the simulations on a GPU and saving the values in a LUT, we were still able to maintain the speed of the inverse algorithm. This two-layer MCLUT method was validated using specially constructed two-layer liquid phantoms where we were able to control the thickness of the top layer. These phantoms were composed of water, polystyrene microspheres for scattering, an absorber in the top layer, and and absorber in the bottom layer. Three different absorbers (red, green, blue), were used, and multiple phantoms were constructed with different combinations of top and bottom absorbers. The results of the validation study were mixed. For specific top layer thicknesses,

we were able to extract the depth dependent optical properties with low levels of error; however, for top layer thickness near 0 μm or greater than 500 μm, the errors were significantly higher. We attributed this to the limited sampling depth of the probe that was used in this study. This realization showed the importance of designing application specific DRS probes that are optimized for specific sampling depths.

In Chapter 4, we looked at the effect of probe geometry and optical properties on sampling depth for diffuse reflectance spectroscopy. Monte Carlo simulation was used to model sampling depth this model was experimentally validated and was shown to accurately predict sampling depth. We then developed an analytical model where sampling depth is expressed in terms of optical properties and probe geometry. This work indicates that for adjacent fiber in the 6-around-1 orientation, the sampling depth cannot be significantly increased by increasing the fiber diameters. This result suggests that deeper sampling depth can only be accomplished by increasing the gap between source and collection fibers. Additionally, the models proposed in Chapter 4 can be used to aid in the design of application specific probes that will be used to interrogate the optical properties of specific layers of tissue such as the epidermis and dermis.

In Chapter 5, we investigated the errors that occur when a one-layer model is used to used to extract properties from a two-layer tissue. This was accomplished by first creating spectra a two-layer model of skin where melanin was confined to the epidermis and hemoglobin was confined to the

dermis. Next, we extracted the properties from the two-layer spectra using an inverse one-layer model. The extracted parameters were then compared to the parameters used to create the two-layer spectra, which allowed us analyze the specific errors caused by the one-layer assumption. We found that using a one-layer model causes an underestimation in hemoglobin concentration and melanin concentration. Additionally, the magnitude of the error is dependent on epidermal thickness. The one-layer assumption also causes an artificial correlation between hemoglobin and melanin concentration. Oxygen saturation is overestimated when it is below 50% and underestimated when it is above 50%. We also found that the vessel radius factor used to account for pigment packaging is correlated with epidermal thickness. These provide strong justification for using a two-layer model when extracting properties from diffuse reflectance spectra collected from skin.

In Chapter 6, we used a custom DRS probe to take skin measurements on 80 subjects at 5 different anatomical locations. Our two-layer MCLUT model was used to extract the properties from the measurements. The extracted properties agreed with published values of skin properties. This promising result shows that DRS has potential to be used for the measurement of depth dependent properties in skin. Future research could extend this dissertation is several ways. For example, the two-layer MCLUT model could be modified to include more complex tissue geometries. This might include adding additional layers or by including a non-layered element to the geometry. The methods described in this dissertation could also be used in a pilot

clinical study for diagnostic purposes.

# Bibliography

[1] Y. N. Mirabal, S. K. Chang, E. N. Atkinson, A. Malpica, M. Follen, and R. Richards-Kortum, "Reflectance spectroscopy for in vivo detection of cervical precancer," *Journal of Biomedical Optics*, vol. 7, no. 4, pp. 587–594, 2002.

[2] G. M. Palmer, Z. Changfang, T. M. Breslin, X. Fushen, K. W. Gilchrist, and N. Ramanujam, "Comparison of multiexcitation fluorescence and diffuse reflectance spectroscopy for the diagnosis of breast cancer," *IEEE Transactions on Biomedical Engineering*, vol. 50, no. 11, pp. 1233–1242, 2003.

[3] D. C. G. de Veld, M. Skurichina, M. J. H. Witjes, R. P. W. Duin, H. J. C. M. Sterenborg, and J. L. N. Roodenburg, "Autofluorescence and diffuse reflectance spectroscopy for oral oncology," *Lasers in Surgery and Medicine*, vol. 36, no. 5, pp. 356–364, 2005.

[4] Y. S. Fawzy, M. Petek, M. Tercelj, and H. Zeng, "In vivo assessment and evaluation of lung tissue morphologic and physiological changes from non-contact endoscopic reflectance spectroscopy for improving lung cancer detection," *Journal of Biomedical Optics*, vol. 11, no. 4, p. 044003, 2006.

[5] I. Georgakoudi, B. C. Jacobson, J. V. Dam, V. Backman, M. B. W. amd

Markus G. M uller, Q. Zhang, K. Badizadegan, D. Sun, G. A. Thomas, L. T. Perelman, and M. S. Feld, "Fluorescence, reflectance, and light-scattering spectroscopy for evaluating dysplasia in patients with barrett's esophagus," *Gastroenterology*, vol. 120, no. 7, pp. 1620–1629, 2001.

[6] G. Zonios, L. T. Perelman, V. Backman, R. Manoharan, M. Fitzmaurice, J. V. Dam, and M. S. Feld, "Diffuse reflectance spectroscopy of human adenomatous colon polyps *in vivo*," *Applied Optics*, vol. 38, no. 31, pp. 6628–6637, 1999.

[7] A. Amelink, A. van der Ploeg van den Heuvel, W. J. de Wolf, D. Robinson, and H. J. C. M. Sterenborg, "Monitoring pdt by means of superficial reflectance spectroscopy," *Journal of Photochemistry and Photobiology B: Biology*, vol. 79, no. 3, pp. 243–251, 2005.

[8] T. J. Farrell, M. S. Patterson, and B. Wilson, "A diffusion-theory model of spatially resolved, steady-state diffuse reflectance for the noninvasive determination of tissue optical-properties *in vivo*," *Medical Physics*, vol. 19, no. 4, pp. 879–888, 1992.

[9] L. Wang, S. L. Jacques, and L. Zheng, "Mcml - monte carlo modeling of light transport in multi-layered tissues," *Computer Methods and Programs in Biomedicine*, vol. 47, no. 2, pp. 131–146, 1995.

[10] R. Hennessy, S. L. Lim, M. K. Markey, and J. W. Tunnell, "Monte carlo lookup table-based inverse model for extracting optical properties from

tissue-simulating phantoms using diffuse reflectance spectroscopy," *Journal of Biomedical Optics*, vol. 18, no. 3, p. 037003, 2013.

[11] M. Sharma, R. Hennessy, M. K. Markey, and J. W. Tunnell, "Verification of a two-layer inverse monte carlo absorption model using multiple source-detector separation diffuse reflectance spectroscopy," *Biomedical Optics Express*, vol. 5, no. 1, pp. 40–53, 2014.

[12] R. Hennessy, W. Goth, M. Sharma, M. K. Markey, and J. W. Tunnell, "Effect of probe geometry and optical properties on the sampling depth for diffuse reflectance spectroscopy," *Journal of Biomedical Optics*, vol. 19, no. 10, p. 107002, 2014.

[13] R. Hennessy, M. K. Markey, and J. W. Tunnell, "Impact of homogeneity assumption on diffuse reflectance spectroscopy of skin," *Journal of Biomedical Optics*, vol. 20, no. 2, p. 027001, 2015.

[14] G. Zonios, J. Bykowski, and N. Kollias, "Skin melanin, hemoglobin, and light scattering properties can be quantitatively assessed *in vivo* using diffuse reflectance spectroscopy," *Journal of Investigative Dermatology*, vol. 117, no. 6, pp. 1452–1457, 2001.

[15] B. W. Murphy, R. J. Webster, B. A. Turlach, C. J. Quirk, C. D. Clay, P. J. Heenan, and D. D. Sampson, "Toward the discrimination of early melanoma from common and dysplastic nevus using fiber optic diffuse reflectance spectroscopy," *Journal of Biomedical Optics*, vol. 10, no. 6, p. 064020, 2005.

[16] U. Utzinger and R. R. Richards-Kortum, "Fiber optic probes for biomedical optical spectroscopy," *Journal of Biomedical Optics*, vol. 8, no. 1, pp. 121–147, 2003.

[17] N. Rajaram, T. H. Nguyen, and J. W. Tunnell, "Lookup table-based inverse model for determining optical properties of turbid media," *Journal of Biomedical Optics*, vol. 13, no. 5, p. 050501, 2008.

[18] B. Nichols, N. Rajaram, and J. W. Tunnell, "Performance of a lookup table-based approach for measuring tissue optical properties with diffuse optical spectroscopy," *Journal of Biomedical Optics*, vol. 17, no. 5, p. 057001, 2012.

[19] G. M. Palmer and N. Ramanujam, "Monte carlo-based inverse model for calculating tissue optical properties. part i: Theory and validation on synthetic phantoms," *Applied Optics*, vol. 45, no. 5, pp. 1062–1071, 2006.

[20] R. Graaff, M. H. Koelink, F. F. M. de Mul, W. G. Zijlstra, A. C. M. Dassel, and J. G. Aarnoudse, "Condensed monte carlo simulations for the description of light transport," *Applied Optics*, vol. 32, no. 4, pp. 426–434, 1993.

[21] E. Tinet, S. Avrillier, and J. M. Tualle, "Fast semianalytical monte carlo simulation for time-resolved light propagation in turbid media," *JOSA A*, vol. 13, no. 9, pp. 1903–1915, 1996.

[22] E. Alerstam, T. Svensson, and S. Andersson-Engels, "Parallel computing with graphics processing unit for high-speed monte carlo simulation of photon migration," *Journal of Biomedical Optics*, vol. 13, no. 6, p. 060504, 2008.

[23] Q. Liu and N. Ramanujam, "Scaling method for fast monte carlo simulation of diffuse reflectance spectra from multilayered turbid media," *JOSA A*, vol. 24, no. 4, pp. 1011–1025, 2007.

[24] L. Wang, S. L. Jacques, and L. Zheng, "Conv - convolution for responses to a finite diameter photon beam incident on multi-layered tissues," *Computer Methods and Programs in Biomedicine*, vol. 54, no. 3, pp. 141–150, 1997.

[25] N. Rajaram, J. S. Reichenberg, M. R. Migden, T. H. Nguyen, and J. W. Tunnell, "Pilot clinical study for quantitative spectral diagnosis of non-melanoma skin cancer," *Lasers in Surgery and Medicine*, vol. 42, no. 10, pp. 716–727, 2010.

[26] M. C. Skala, G. M. Palmer, K. M. Vrotsos, A. Gendron-Fitzpatrick, and N. Ramanujam, "Comparison of a physical model and principal component analysis for the diagnosis of epithelial neoplasias *in vivo* using diffuse reflectance spectroscopy," *Optics Express*, vol. 15, no. 12, pp. 7863–7875, 2007.

[27] S. Wan, R. R. Anderson, and J. A. Parrish, "Analytical modeling for

the optical properties of the skin with in vitro and in vivo applications," *Photochemistry and Photobiology*, vol. 34, no. 4, pp. 493–499, 1981.

[28] G. Zonios, I. Bassukas, and A. Dimou, "Comparative evaluation of two simple diffuse reflectance models for biological tissue applications," *Applied Optics*, vol. 47, no. 27, pp. 4965–4973, 2008.

[29] T. Papaioannou, N. W. Preyer, F. Qiyin, A. Brightwell, M. Carnohan, G. Cottone, R. Ross, L. R. Jones, and L. Marcu, "Effects of fiber-optic probe design and probe-to-target distance on diffuse reflectance measurements of turbid media: an experimental and computational study at 337 nm," *Applied Optics*, vol. 43, no. 14, pp. 2846–2860, 2004.

[30] T. J. Farrell, B. C. Wilson, and M. S. Patterson, "The use of a neural network to determine tissue optical properties from spatially resolved diffuse reflectance measurements," *Physics in Medicine and Biology*, vol. 37, no. 12, pp. 2281–2286, 1992.

[31] A. Kienle, L. Lilge, M. S. Patterson, R. Hibst, R. Steiner, and B. C. Wilson, "Spatially resolved absolute diffuse reflectance measurements for noninvasive determination of the optical scattering and absorption coefficients of biological tissue," *Applied Optics*, vol. 35, no. 13, pp. 2304–2314, 1996.

[32] T. J. Farrell, M. S. Patterson, and M. Essenpreis, "Influence of layered tissue architecture on estimates of tissue optical properties obtained

from spatially resolved diffuse reflectance reflectometry," *Applied Optics*, vol. 37, no. 10, pp. 1958–1972, 1998.

[33] I. S. Seo, J. S. You, C. K. Hayakawa, and V. Venugopalan, "Perturbation and differential monte carlo methods for measurement of optical properties in a layered epithelial tissue model," *Journal of Biomedical Optics*, vol. 12, no. 1, p. 014030, 2007.

[34] G. Mantis and G. Zonios, "Simple two-layer reflectance model for biological tissue applications," *Applied Optics*, vol. 48, no. 18, pp. 3490–3496, 2009.

[35] G. Zonios and A. Dimou, "Simple two-layer reflectance model for biological tissue applications: lower absorbing layer," *Applied Optics*, vol. 49, no. 27, pp. 5026–5031, 2010.

[36] T. Y. Tseng, C. Y. Chen, Y. S. Li, and K. B. Sung, "Quantification of the optical properties of two-layered turbid media by simultaneously analyzing the spectral and spatial information of steady-state diffuse reflectance spectroscopy," *Biomedical Optics Express*, vol. 2, no. 4, pp. 901–914, 2011.

[37] Q. Liu and N. Ramanujam, "Sequential estimation of optical properties of a two-layered epithelial tissue model from depth-resolved ultraviolet-visible diffuse reflectance spectra," *Applied Optics*, vol. 45, no. 19, pp. 4476–4490, 2006.

[38] A. Kienle, M. S. Patterson, N. Dögnitz, R. Bays, G. Wagnieres, and H. van den Bergh, "Noninvasive determination of the optical properties of two-layered turbid media," *Applied Optics*, vol. 37, no. 4, pp. 779–791, 1998.

[39] D. Yudovsky and L. Pilon, "Rapid and accurate estimation of blood saturation, melanin content, and epidermis thickness from spectral diffuse reflectance," *Applied Optics*, vol. 49, no. 10, pp. 1707–1719, 2010.

[40] F. Alizadeh, "Interior point methods in semidefinite programming with applications to combinatorial optimization," *SIAM Journal of Optimization*, vol. 5, no. 1, pp. 13–51, 1995.

[41] E. Borisova, P. Troyanova, P. Pavlova, and L. Avramov, "Diagnostics of pigmented skin tumors based on laser-induced autofluorescence and diffuse reflectance spectroscopy," *Quantum Electronics*, vol. 38, no. 6, p. 597, 2008.

[42] G. Zonios, A. Dimou, M. Carrara, and R. Marchesini, "*In vivo* optical properties of melanocytic skin lesions: common nevi, dysplastic nevi and malignant melanoma," *Photochemistry and Photobiology*, vol. 86, no. 1, pp. 236–240, 2010.

[43] Z. Ge, K. T. Schomacker, and N. S. Nishioka, "Identification of colonic dysplasia and neoplasia by diffuse reflectance spectroscopy and pattern recognition techniques," *Applied Spectroscopy*, vol. 52, no. 6, pp. 212A–229A, 1998.

[44] F. Koenig, R. Larne, H. Enquist, F. J. McGovern, K. T. Schomacker, N. Kollias, and T. F. Deutsch, "Spectroscopic measurement of diffuse reflectance for enhanced detection of bladder carcinoma," *Urology*, vol. 51, no. 2, pp. 342–345, 1998.

[45] N. M. Marín, A. Milbourne, H. Rhodes, T. Ehlen, D. Miller, L. Benedet, R. Richards-Kortum, and M. Follen, "Diffuse reflectance patterns in cervical spectroscopy," *Gynecologic Oncology*, vol. 99, no. 3, pp. S116–S120, 2005.

[46] H. Arimoto, M. Egawa, and Y. Yamada, "Depth profile of diffuse reflectance near-infrared spectroscopy for measurement of water content in skin," *Skin Research and Technology*, vol. 11, no. 1, pp. 27–35, 2005.

[47] A. J. Gomes and V. Backman, "Algorithm for automated selection of application-specific fiber-optic reflectance probes," *Skin Research and Technology*, vol. 18, no. 2, p. 027012, 2013.

[48] Y. Tsuchiya, "Photon path distribution and optical responses of turbid media: theoretical analysis based on the microscopic beer-lambert law," *Physics in Medicine and Biology*, vol. 46, no. 8, pp. 2067–2084, 2001.

[49] X. Guo, M. F. G. Wood, and A. Vitkin, "A monte carlo study of penetration depth and sampling volume of polarized light in turbid media," *Optics Communications*, vol. 281, no. 3, pp. 380–387, 2008.

[50] S. C. Kanick, D. J. Robinson, H. J. C. M. Sterenborg, and A. Amelink, "Monte carlo analysis of single fiber reflectance spectroscopy: photon path length and sampling depth," *Physics in Medicine and Biology*, vol. 54, no. 22, pp. 6991–7008, 2009.

[51] A. J. Gomes, V. Turzhitsky, S. Ruderman, and V. Backman, "Monte carlo model of the penetration depth for polarization gating spectroscopy: influence of illumination-collection geometry and sample optical properties," *Applied Optics*, vol. 51, no. 20, pp. 4627–4637, 2012.

[52] A. J. Gomes and V. Backman, "Analytical light reflectance models for overlapping illumination and collection area geometries," *Applied Optics*, vol. 51, no. 33, pp. 8013–8021, 2013.

[53] C. Bonnéry, P.-O. Leclerc, M. Desjardins, R. Hoge, L. Bherer, P. Pouliot, and F. Lesage, "Changes in diffusion path length with old age in diffuse optical tomography," *Journal of Biomedical Optics*, vol. 17, no. 5, p. 056002, 2012.

[54] S. C. Kanick, H. J. C. M. Sterenborg, and A. Amelink, "Empirical model description of photon path length for differential path length spectroscopy: combined effect of scattering and absorption," *Journal of Biomedical Optics*, vol. 13, no. 6, p. 064042, 2008.

[55] E. Alerstam, W. C. Y. Lo, T. D. Han, J. Rose, S. Andersson-Engels, and L. Lilge, "Next-generation acceleration and code optimization for light

transport in turbid media using gpus," *Biomedical Optics Express*, vol. 1, no. 2, pp. 658–675, 2010.

[56] K. W. Calabro and I. J. Bigio, "Influence of the phase function in generalized diffuse reflectance models: review of current formalisms and novel observations," *Journal of Biomedical Optics*, vol. 19, no. 7, p. 075005, 2014.

[57] T. Gambichler, R. Matip, G. Moussa, P. Altmeyer, and K. Hoffmann, "*In vivo* data of epidermal thickness evaluated by optical coherence tomography: effects of age, gender, skin type, and anatomic site," *Journal of Dermatological Science*, vol. 44, no. 3, pp. 145–152, 2006.

[58] G. N. Stamatas, B. Z. Zmudka, N. Kollias, and J. Z. Beer, "*In Vivo* measurement of skin erythema and pigmentation: New means of implementation of diffuse reflectance spectroscopy with a commercial instrument," *British Journal of Dermatology*, vol. 159, no. 3, pp. 683–690, 2008.

[59] L. Lim, B. Nichols, N. Rajaram, and J. W. Tunnell, "Probe pressure effects on human skin diffuse reflectance and fluorescence spectroscopy measurements," *Journal of Biomedical Optics*, vol. 16, no. 1, p. 011012, 2011.

[60] S. Tseng, A. Grant, and A. J. Durkin, "*In Vivo* determination of skin near-infrared optical properties using diffuse optical spectroscopy," *Journal of Biomedical Optics*, vol. 13, no. 1, p. 014016, 2008.

[61] A. Garcia-Uribe, E. B. Smith, J. Zou, M. Duvic, V. Prieto, and L. Wang, "*In Vivo* characterization of optical properties of pigmented skin lesions including melanoma using oblique incidence diffuse reflectance spectroscopy," *Journal of Biomedical Optics*, vol. 16, no. 2, p. 020501, 2011.

[62] G. Zonios, A. Dimou, I. Bassukas, D. Galaris, A. Tsolakidis, and E. Kaxiras, "Melanin absorption spectroscopy: New method for noninvasive skin investigation and melanoma detection," *Journal of Biomedical Optics*, vol. 13, no. 1, p. 014017, 2008.

[63] R. M. P. Doornbos, R. Lang, M. C. Aalders, F. W. Cross, and H. J. C. M. Sterenborg, "The determination of *In Vivo* human tissue optical properties and absolute chromophore concentrations using spatially resolved steady-state diffuse reflectance spectroscopy," *Physics in Medicine and Biology*, vol. 44, no. 4, pp. 967–981, 1999.

[64] C. Zhu, G. M. Palmer, T. M. Breslin, J. Harter, and N. Ramanujam, "Diagnosis of breast cancer using diffuse reflectance spectroscopy: Comparison of a monte carlo versus partial least squares analysis based feature extraction technique," *Lasers in Surgery and Medicine*, vol. 38, no. 7, pp. 714–724, 2006.

[65] I. Fredriksson, M. Larsson, and T. Strömberg, "Inverse monte carlo method in a multilayered tissue model for diffuse reflectance spectroscopy," *Journal of Biomedical Optics*, vol. 17, no. 4, p. 047004, 2012.

[66] X. Zhong, X. Wen, and D. Zhu, "Lookup-table-based inverse model for human skin reflectance spectroscopy: Two-layered monte carlo simulations and experiments," *Optics Express*, vol. 22, no. 2, pp. 1852–1864, 2014.

[67] S. L. Jacques, R. D. Glickman, and J. A. Schwartz, "Internal absorption coefficient and threshold for pulsed laser distribution of melanosomes isolated from retinal pigment epithelium," *Proceedings of SPIE*, vol. 2681, pp. 468–477, 1996.

[68] S. A. Prahl, "Optical absorption of hemoglobin," *http://omlc.ogi.edu/spectra/hemoglobin/*, Accessed Aug 2014.

[69] T. Lister, P. A. Wright, and P. H. Chappell, "Optical properties of human skin," *Journal of Biomedical Optics*, vol. 17, no. 9, p. 090901, 2012.

[70] R. L. van Veen, W. Verkuysse, and H. J. Sterenborg, "Diffuse-reflectance spectroscopy from 500 to 1060 nm by correction for inhomogeneously distributed absorbers," *Optics Letters*, vol. 27, no. 4, pp. 246–248, 2002.

[71] A. Amelink, J. Haringsma, and H. J. C. M. Sterenborg, "Noninvasive measurement of oxygen saturation of the microvascular blood in barrett's dysplasia by use of optical spectroscopy," *Gastrointestinal Endoscopy*, vol. 70, no. 1, pp. 1–6, 2009.

[72] A. Amelink, A. P. van den Heuvel, W. J. de Wolf, D. J. Robinson, and H. J. C. M. Sterenborg, "Monitoring pdt by means of superficial re-

flectance spectroscopy," *Journal of Photochemistry and Photobiology B*, vol. 79, no. 3, pp. 243–251, 2005.

[73] M. P. L. Bard, A. Amelink, M. Skurichina, G. N. Hegt, R. P. Duin, H. J. C. M. Sterenborg, H. C. Hoogsteden, and J. G. Aerts, "Optical spectroscopy for the classification of malignant lesions of the bronchial tree," *Chest*, vol. 129, no. 4, pp. 995–1001, 2006.

[74] T. K. Lee, E. D. baron, and T. H. Foster, "Monitoring pc 4 photodynamic therapy in clinical trials of cutaneous t-cell lymphoma using noninvasive spectroscopy," *Journal of Biomedical Optics*, vol. 13, no. 3, p. 030507, 2008.

[75] D. Arifler, C. MacAulay, M. Follen, and R. Richards-Kortum, "Spatially resolved reflectance spectroscopy for diagnosis of cervical precancer: Monte carlo modeling and comparison to clinical measurements," *Journal of Biomedical Optics*, vol. 11, no. 6, p. 064027, 2006.

[76] F. Foschum and A. Kienle, "Broadband absorption spectroscopy of turbid media using a dial step stead-state method," *Journal of Biomedical Optics*, vol. 17, no. 3, p. 037009, 2012.

[77] S.-H. Tseng, P. Bargo, A. Durkin, and N. Kollias, "Chromophore concentrations, absorption and scattering properties of human skin *in vivo*," *Optics Express*, vol. 17, no. 17, pp. 14599–14617, 2009.

[78] D. Hattery, B. Hattery, V. Chernomordik, P. Smith, M. Loew, J. Mulshine, and A. Gandjbakhche, "Differential oblique angle spectroscopy of the oral epithelium," *Journal of Biomedical Optics*, vol. 9, no. 5, pp. 951–960, 2004.

[79] R. J. Nordstrom, L. Burke, J. M. Niloff, and J. F. Myrtle, "Identification of cervical intraepithelial neoplasia (cin) using uv-excited fluorescence and diffuse-reflectance tissue spectroscopy," *Lasers in Surgery and Medicine*, vol. 29, no. 2, pp. 118–127, 2001.

[80] R. Marbach, T. Koschinsky, F. A. Gries, and H. M. Heise, "Noninvasive blood glucose assay by near-infrared diffuse reflectance spectroscopy of the human inner lip," *Applied Spectroscopy*, vol. 47, no. 7, pp. 875–881, 1993.

[81] D. Contini, F. Martelli, and G. Zaccanti, "Photon migration through a turbid slab described by a model based on diffusion approximation. i. theory," *Applied Optics*, vol. 36, no. 19, pp. 4587–4599, 1997.

[82] K. M. Yoo, F. Liu, and R. R. Alfano, "When does the diffusion approximation fail to describe photon transport in random media?," *Physical Review Letters*, vol. 64, no. 22, pp. 2647–2650, 1990.

[83] S. Nouveau-Richard, M. Monot, P. Bastien, and O. de Lacharrière, "*In vivo* epidermal thickness measurement: ultrasound vs. confocal imaging," *Skin Research and Technology*, vol. 10, no. 2, pp. 136–140, 2004.

[84] F. Bevilacqua and C. Depeursinge, "Monte carlo study of diffuse reflectance at source–detector separations close to one transport mean free path," *JOSA A*, vol. 16, no. 12, pp. 2935–2945, 1999.

[85] J. C. Finlay and T. H. Foster, "Effect of pigment packaging on diffuse reflectance spectroscopy of samples containing red blood cells," *Optics Letters*, vol. 29, no. 9, pp. 965–967, 2004.

[86] R. H. Bremmer, A. Nadort, T. G. van Leeuwen, M. J. C. van Gemert, and M. C. G. Aalders, "Age estimation of blood stains by hemoglobin derivative determination using reflectance spectroscopy," *Forensic Science International*, vol. 206, no. 1-3, pp. 167–171, 2011.

[87] M. D. Keller, S. K. Majumder, M. C. Kelley, I. M. Meszoely, F. I. Boulos, G. M. Olivares, and A. Mahadevan-Jansen, "Autofluorescence and diffuse reflectance spectroscopy and spectral imaging for breast surgical margin analysis," *Lasers in Surgery and Medicine*, vol. 42, no. 1, pp. 15–23, 2010.

[88] N. Kollias, A. Baqer, and I. Sadiq, "Minimum erythema dose determination in individuals of skin type v and vi with diffuse reflectance spectroscopy," *Photodermatology, Photoimmunology and Photomedicine*, vol. 10, no. 6, pp. 249–254, 1994.

[89] M. Donoso, D. O. Kildsig, and E. S. Ghaly, "Prediction of tablet hardness and porosity using nearinfrared diffuse reflectance spectroscopy as a nondestructive method," *Pharmaceutical Development and Technology*, vol. 8, no. 4, pp. 357–366, 2003.

[90] R. R. Anderson and J. A. Parrish, "The optics of human skin," *Journal of Investigative Dermatology*, vol. 77, no. 1, pp. 13–19, 1981.

[91] S. V. Patwardhan, A. P. Dhawan, and P. A. Relue, "Monte carlo simulation of light-tissue interaction: Three-dimensional simulation for transillumination based imaging of skin lesions," *IEEE Transactions on Biomedical Engineering*, vol. 52, no. 7, pp. 1227–1236, 2005.

[92] R. Marchesini, C. Clemente, E. Pignolia, and M. Brambilla, "Optical properties of in vitro epidermis and their possible relationship with optical properties of in vivo skin," *Journal of Photochemistry and Photobiology B: Biology*, vol. 16, no. 2, pp. 127–140, 1992.

[93] E. Salomatina, B. Jiang, J. Novak, and A. N. Yaroslavsky, "Optical properties of normal and cancerous human skin in the visible and near-infrared spectral range," *Journal of Biomedical Optics*, vol. 11, no. 6, p. 064026, 2006.